Università degli Studi di Napoli
Federico II
Dipartimento di Scienze Fisiche

Tesi di Dottorato in Fisica Fondamentale ed Applicata

Statistical mechanical approach to the study of Eukaryotic Directional Sensing

Teresa Ferraro

Tutor:
Chiar.mo Prof. A. Coniglio

Coordinatore:
Chiar.mo Prof. L. Marrucci

XXI ciclo 2005-2008

Contents

Introduction

In recent years the role of physical methodologies and models is becoming important in the study of Biology. The biological process are often very complex and Statistical Physics offer a synthetic picture and explanation of many behaviors. Statistical physics has the peculiarity to explain the emergence of complex behaviors from simplified models of microscopic interactions combining statistical principles and dynamical laws.

In this work we show a Statistical Mechanics approach to the study of Eukaryotic Directional Sensing. Many eukaryotic cells are able to orient (polarize) in order to move along a given direction in presence of an external stimulation (chemotaxis). This process is fundamental for important biological functions like morphogenesis of organs and tissues, wound healing, immune response, social behavior of some ameboid cells. It involves different kind of eukaryotic cells: cells involved in the immune system, endothelial cells, amphibian eggs, amoebas. This is an indication that the process of directional sensing is a universal phenomenon. The process of orientation consists in the pattern formation of domains of two different enzymes determining a symmetry breaking which triggers the directional sensing [11]. Pattern formation happens in answer to an external stimulation, usually a chemical signal, that activates specific receptors on cell surface and it is produced by a cascade of chemical reactions leading to the cell polarization [4]. Experimental observations [15] suggest that the domains formation is a consequence of self-organization of molecules patches.

It is natural, from a physical point of view, to represent the phenomenon like a self-organized phase ordering process, where the cell state, spontaneously, or driven by an anisotropic external field, decays into a state of coexistence of two or more chemical phases, spatially localized in different regions in order to define a front and a rear. We model the process by associating a lattice to the cell surface populated by a spin variable whose values identifies the enzymes. An effective free energy regulates the interactions of the enzymes with the external chemical source and with a cytosolic reservoir. The free energy is able to create the conditions of phase coexistence

necessary for the phase separation process [23].

The synthetic description derived from a free energy approach offer the possibility of a general treatment of the Hamiltonian considered for the lattice model. We study the Hamiltonian as a continuous Landau-Ginzburg functional in the framework of large N model. The order parameter represents, in the scalar limit, the concentration difference of the enzymes. The large N limit is a powerful method of the Statistical Mechanics which yield the possibility to obtain analytical results. We study numerically and analytically the Langevin equation of motion deriving the phase diagram and the time behavior of magnetization and structure factor.

The last part of this thesis is devoted to the study of the effect of chemotaxis on the dynamical process of cells aggregation in the morphogenesis of simulated vascular networks. Experiments shows [42] that chemotaxis plays an important role in the formation of vascular networks in vitro. The de novo growth of the primary vascular network from initially endothelial cells is called Vasculogenesis and it is the first step in the development of the circulatory system in vertebrates. The endothelial cells produce a chemical factor which degrades in time creating local gradients which guides the cell chemotaxis. The cells autorganize in networks structure showing, during the aggregation, the characteristics of a percolation process [40]. The formed networks have self-similar structure which can give information about the dynamical aggregation process from the study of the fractal dimension. It is possible to associate an effective interaction length to the chemical factor. Our purpose is to investigate the role of the effective interaction length on the fractal behavior of simulated two-dimensional vascular networks. We performed Monte Carlo simulations by using the Cellular Potts Model [37, 38, 39], a lattice-gas model, where the endothelial cells are represented by spins of Potts and the chemical factor is represented as continuous concentration field around the cells. From the study of different structures, obtained by varying the effective radius of attractant, it appears clearly that, for scales close to the radius, the chemical soluble factor determines the dynamical process of aggregation and for larger scale the shape of structures is influenced only by the initial random position of cells.

The thesis is organized in five chapters. In the first chapter we describe the biological characteristic of eukaryotic directional sensing and summarize the main models previously used for the process. In the second chapter we illustrate and discuss the spin lattice model. The chapters 3 and 4 are devoted to the study of the free energy in the large N limit. Finally the chapter 5 contains the study of the fractal behavior of simulated vascular networks.

Chapter 1

The eukaryotic directional sensing

1.1 Introduction

Animals, plants, fungi are constituted by eukaryotic cell. The word eukaryote comes from the Greek $\epsilon\upsilon$ (eu), meaning "good", and $\kappa\alpha\rho\upsilon o\nu$ (karyon), "nut". They have this name because they have membrane-bounded nucleus, enclosing DNA, which differentiates eukaryotic cells from prokaryotic cells (bacterias) which doesn't have a nucleus. Until 1800 millions of years ago, our planet had only procaryotic living organisms. Probably the first eukaryotic cell was created thanks to the cooperation between two bacterias; one of them incorporated another creating a cell with a nucleus. After millions of years of evolution we observe our complex eukaryotic cells.

The simplest form of life is a solitary cell that reproduces by binding in two. Higher organisms are like cellular cities, in which groups of cell perform specialized functions and are linked by intricate systems of communication. The living Eukaryotic cell is itself a little universe where fascinating phenomena happen.

In the nucleus of a single cell there is the DNA, which contains all the genetic code of the eukaryotic organism. A single cell can read and use the genetic information, it can breathe, it can communicate with other cells, and many eukaryotic cells can detect external stimulation, establish a direction and move along it. Eukaryotic cells are unique in containing a cytoskeleton of protein filaments that help to organize cytoplasm and provide the machinery for movement.

Specific moments of the life of a cell living in a multicellular community, such as migration, proliferation, organization in layers or complex tissues,

imply spatial organization along some axis of direction. The original spatial symmetry of the cell must be broken to adapt to a highly structured anisotropic environment. Many eukaryotic cells respond with directional movement to spatial and temporal gradients of small molecules that bind to cell surface. This process, called chemotaxis, is crucial in many biological functions: immune response of higher animals, wound healing, neuronal patterning, vascular and embryonic development, as well as the food gathering and social behavior of some amoeboid cells. For instance, migrating cells must orient towards sources of chemical attractants, mitotic cells must orient along the spindle-pole axis to bud daughter cells, epithelial cells must recognize the inner and outer part of tissues to define organ boundaries. In

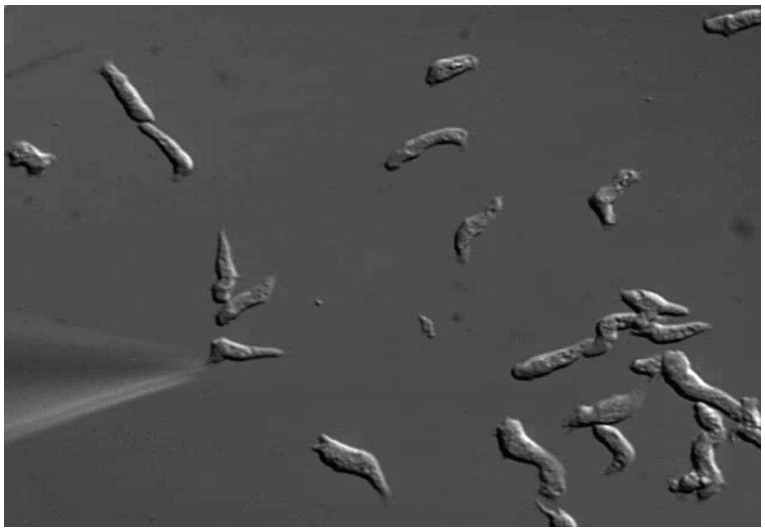

Figure 1.1: The image shows Dictyostelium discoideum cells chemotaxing towards a micropipette emitting the chemoattractant cAMP. The Dictyostelium discoideum is a species of soil-living amoeba. It is a primitive eukaryote that has been widely used to study the mechanisms of cell movement, chemotaxis and cell signaling.

this thesis we will present a model of Eukaryotic Directional Sensing based on standard Statistical Mechanics methods.

1.2 Chemotaxis

Chemotaxis is possible after polymerization of the actin filaments which are the main constituents of cytoskeleton. Actin is a globular protein that as-

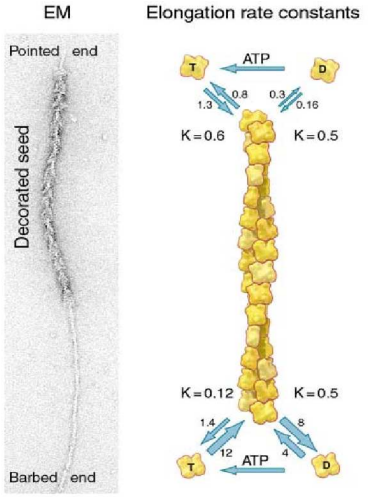

Figure 1.2: Actin Filament Elongation and ATP Hydrolysis. The EM (Electronic Microscopy) shows an actin filament seed decorated with myosin heads and elongated with ATP-actin. The association rate constants have units of $\mu M^{-1}s^{-1}$. Dissociation rate constants have units of s^{-1}. The ratio of the dissociation rate constant to the association rateconstant gives K, the dissociation equilibrium constant with units of μM. Note that the equilibrium constants for ATP-actin differ at the two ends, giving rise to slow steady state treadmilling. By Pollard et al. [19].

sembles into biopolymers with filamentous structures with two structurally distinct ends. The monomers are called globular actin (G-actin) and the filaments are called F-actin. The two distinct ends are a fast and slow growing end (called the plus and minus end respectively). Polarity of actin filaments is based on molecular polarity of G-actin which has an arrowhead pattern created by decoration with myosin, an important protein which participate with actin to create the cytoskeletal mesh[20]. The first step in actin polimerization is the Nucleation actin trimer from G-actin monomers. This process is very slow, probably because the actin monomers have to combine in a precise conformation of trimers. After nucleation, filaments grow rapidly. The actin monomers stores energy including of ATP nucleotide. The trimer structure is stable and after the addition of an actin monomer hydrolysis of ATP in ADP occours. This process is important to preserve polarity for actin filaments. Infact the ATP hydrolysis polarize the actin filaments in terms of polymerization rates in two ends. The ATP-containing end (plus end) is more stable against depolymerization and grows more quickly, whereas

the ADP-containing and (minus end) is less likely to bind a monomer and grows slowly Fig. 1.2. Polymerization proceeds until the concentration of free monomers is below the critical concentration for growth the minus end, but above that the plus end. The cell can therefore regulate actin polymerization by varying the availability of ATP. The minus end has a critical actin monomer concentration that is ~ 6 times higher than that at plus ends.

The polar structure of actine filaments endows the actin cytoskeleton with directionality on macroscopic scales. When the end of an actin filament (AF) is exposed to a concentration of monomeric actin that is above its critical concentration, the filament end binds monomers and grows by polymerization. Conversely, when the concentration is below the critical concentration, monomers detach from the filament end, and the filament shrinks by depolymerization. Simply by having these two different critical actin concentrations at the opposing ends of the filament, AFs can grow asymmetrically, and when the actin monomer concentration lies between the two values, only the plus end grows while the minus end shrinks. This process, where the length of the filament stays roughly constant and the polymerized monomers within the AF transfer momentum forward due to asymmetric plus end polymerization, is known as treadmilling. In this way a dynamic process emerges, where although there is no net growth, there is a net flux of monomers trough the filament. It is a critical aspect of how polymerizing AFs can generate force and it is important for the spreading as well as the directional movement of cells.

Once cell movement begins, the process, which involves the constant restructuring of the actin cytoskeleton, can be divided into three stages in most cells Fig. 1.3. First, a cell propels the membrane forward by orienting and reorganizing (growing) the actin network at its leading edge. Second, it adheres to the substrate at the leading edge and deadheres (releases) at the cell body and rear of the cell. Finally, contractile forces, generated largely by the action of the acto-myosin network, pull the cell forward.

A cell begins to move in response to an external signal in its surrounding environment. This can be a physical, chemical, diffusive or non-diffusive signal that is detected by receptor proteins located on the cell membrane, and transmitted by them via signaling cascades to the cell interior. During directional sensing cells transduce the external distribution of chemotactic ligand into an internal distribution of signaling molecules that effect, by a not yet well known cascade of chemical reactions, the morphological and mechanical changes necessary for movement.

Cytoskeleton dynamics can be decoupled from directional sensing by use of inhibitors of actin polymerization so that cells are immobilized but respond with the some behavior of signaling molecules of untreated cells [1]. Than

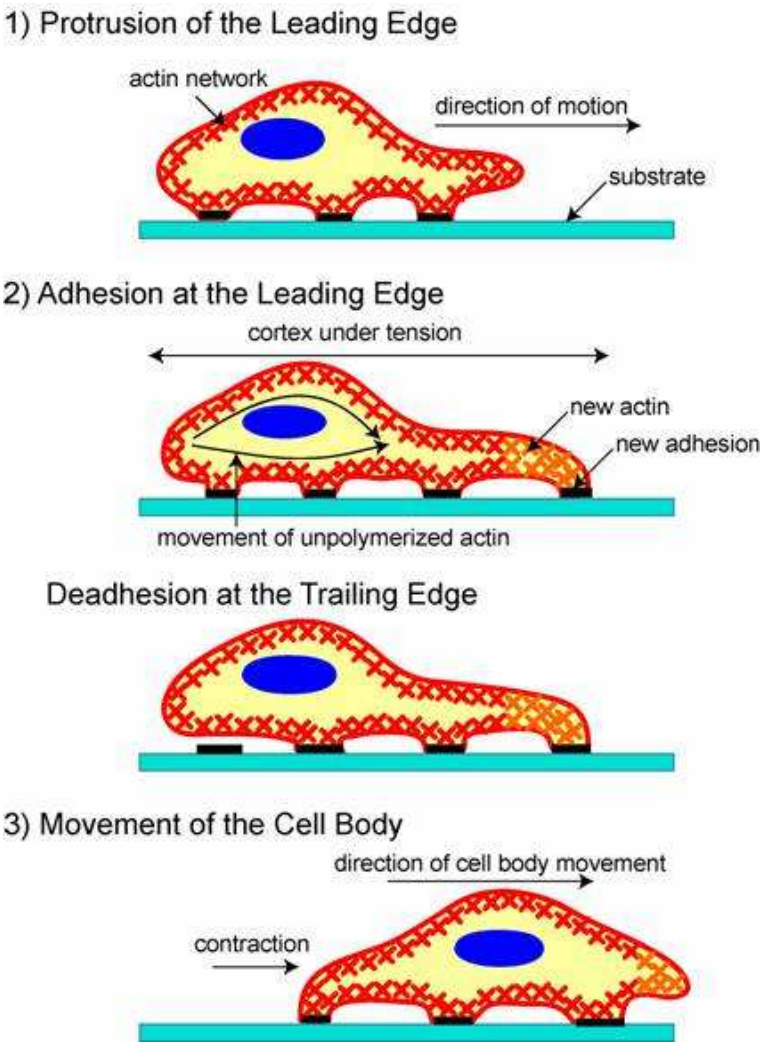

Figure 1.3: A schematic of the three stages of cell movement. After determining its direction of motion, the cell extends a protrusion in this direction by actin polymerization at the leading edge. It then adheres its leading edge to the surface on which it is moving and de-adheres at the cell body and rear. Finally, it pulls the whole cell body forward by contractile forces generated at the cell body and rear of the cell. By Ananthakrishnan [24].

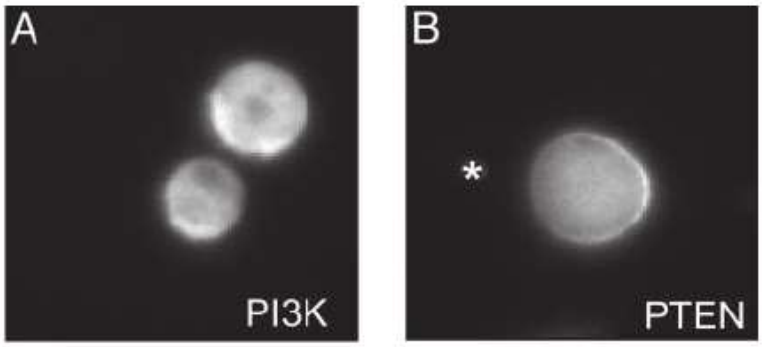

Figure 1.4: Response in fluorescence level of PIK3 enzymes (A) or PTEN (B) under varying chemotactic gradients. (A Upper) The pipette is located 10 μm below the bottom-left corner of the frame; (B) the location is denoted by the asterisk. By Janetopoulos et al. [1].

it is possible to treat the directional sensing separately from the cytoskeletal dynamic. In this thesis we focus on the phenomenon of directional sensing which break the symmetry of cell membrane.

1.3 The biological mechanism of directional sensing

During last years, there had been many experimental observations clarifying the biological mechanism in directional sensing.

The general picture emerging from the analysis of chemotaxis in several different eukaryotic cell types indicates that the process evolves two enzymes on their phospholipid products [1]. The enzyme phosphatidylinositol 3-kinase (PI3K) and his product the trisphosphate (PIP_3) phospholipid, and phosphatase and tensin homolog enzyme (PTEN) with its bisphosphate (PIP_2) phospholipide play the major role in the process.

An oriented cell shows a strong accumulation of PI3K and PIP_3 at leading edge whereas the most part of PTEN and PIP_2 is located at the side of cell membrane. If the chemoattractant has a gradient, cells respond with strong accumulation of the enzyme PI3K and its product PIP_3 on the plasma membrane side exposed to the highest concentration of chemoattractant whereas the PTEN enzyme and its product PIP_2 accumulates on the opposite side Fig. 1.4. PI3K catalyze the switch of the phospholipid bisphosphate PIP_2 in the trisphosphate PIP_3 states, conversely, the PTEN catalyze PIP_3 in PIP_2.

The phospholipids are permanently bound to the inner face of the cell membrane, while the two enzymes diffuse in the cell volume and become active when they are adsorbed on the membrane. PI3K adsorption takes place through binding to receptors of the external attractant. PTEN adsorption takes place through binding to the PTEN product, PIP_2, a process which introduces an amplification loop in the system dynamics [6, 4]. A second amplification loop provided by PI3K binding to PIP_3 has been recently observed [7].

The discovery of new proteins and agents add particulars and new questions to the biochemical intracellular picture of directional sensing but the observed phenomenon at cell level is well studied and shows very interesting characteristics, as we describe in the following paragraph.

1.3.1 Characteristics of directional sensing.

In presence of a shallow gradient of chemoattractant the phosphoinsitide and enzyme distributions do not simply mirror the receptor activation gradient, but rather a strong and sharp separation in PIP_2-PTEN and PIP_3-PI3K-rich zones arises. The process works as an efficient gradient amplifier: a few percent gradient ($\sim$ 2 %) is sufficient to completely polarize the cell membrane.

The eukaryotic cells have no a priori directionality, as consequence we observe that orientation response is reversible: by inverting the gradient direction the orientation is also inverted. In Fig.1.5 the changing of distribution of PIP_3 molecules is showed. This characteristic has an important consequence on the cell mobility. Infact also the directional motion of cells inverts its direction, giving the possibility to the cell to adapt in the time to the changes of the external stimuli. In Fig.1.6 is showed the reorientation of a populations of rabbit neutrophylis after the gradient inversion.

Two different regimes of membrane polarization may be distinguished: in presence of gradient of stimulant and with a uniform stimulant. In the presence of an attractant gradient, anisotropy driven polarization is realized in a time of the order of a few minutes, and results in the formation of a PI3K-rich patch on the membrane side closer to the attractant source and of a PTEN-rich patch in the complementary region [6]. On the other hand, cells exposed to uniform distributions of attractant polarize in random directions over a longer timescale.

The average concentration of attractant is of crucial importance, as shown by experimentally observed dose-response curves [8] Fig. 1.7. The directional sensing takes places for a wide range of chemoattractant concentration, this range can variate with the cell type and the kind of attractant but there

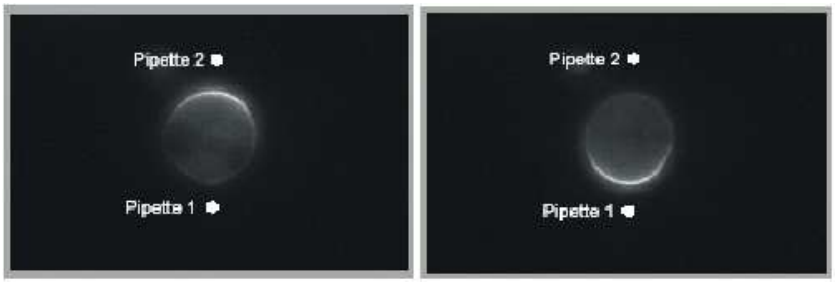

Figure 1.5: Eukaryotic cells are equally responsive at all points on their perimeters. Discoideum cells expressing PHCrac-GFP (indicator of PIP_3 presence) sense a gradient of cAMP released from a micropipette. By fluorescence the cell on the right shows concentration of PIP_3 binding to the membrane on the side of the cell exposed to gradient emanating from pipette 1 (dot), and then rapidly (within 60 s) translocates to the other side when pipette 2 (dot) is turned on (left). By Devreotes et al. [14].

are at least two-three order of magnitude of concentration of attractant that enhance the directional sensing and chemotaxis. Directional sensing does not take place neither at very low nor at very high attractant levels, and there exists an optimal attractant concentration such that the cell response is maximal.

Postma and coworkers [15] observe that, after a chemical stimulation, the cell surface show the presence of domains of PHCrac-GFP characterized by the presence of PIP_3. The PIP_3 triggers the formation of PHCrac-GFP domains which are the activated zone for the actin polymerization as in Fig.1.8. The characteristic that seems to emerge from this experiment is that the spatial organizing of phosphoinositides (and enzymes) is driven by a self-organization of signaling patches.

Once there is establishment of cell polarity, the lipid PIP_3, accumulates at the leading edge of chemotacting cells, induces actin polymerization and protrusions like pseudopoda extension, triggering the cell chemotaxis.

1.4 Directional sensing models

A number of theoretical models have been proposed to explore different potential mechanisms for gradient sensing and polarization [18]. They attempt to explain the ability of cells to generate, amplified persistent intra-cellular responses to external chemoattractants. The most part of them hypothesize a mechanism and describe the process using coupled differential equations as

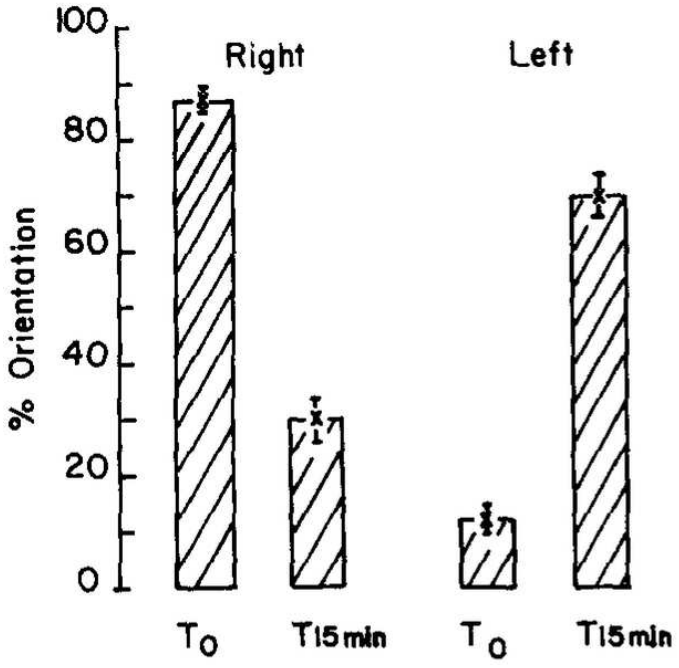

Figure 1.6: Reversibility in cell motility. Rabbit neutrophila cells were stimulated for orientation in the right direction. The attractant fluid was then removed and replaced with fresh medium with the direction of the gradient reversed. After 15 min the reversal the most part of cells is oriented in the new direction. By Zigmond [8].

method to compute the distributions of molecules evolved in the the process (see for a review[18]) to mimic the signaling moulecules responce of the cell.

Several models are based on a local excitation of signaling moulecules (PIP_3, PTEN, PH domains) and a global inhibition principle (LEGI mechanism) Fig.1.9. The activator binds to the membrane at a rate proportional to the local degree of receptor activation. The inhibitor, on the other hand, responds to the integrated receptor activity. Its activity, therefore is proportional to the average concentration of attractant across length of cell. The cell determines its front and rear by comparing the local concentration of the activator on the membrane relative to the global concentration of the inhibitor. Qualitatively, the LEGI mechanism can account for the observed gradient sensing response of most of the molecules that have been shown in neutrophils and Dictyostelium cells to translocate to or be activated transiently on the cell cortex during uniform stimulation and move to or be activated at the front (like PI3K, PH domains, actin binding proteins) or

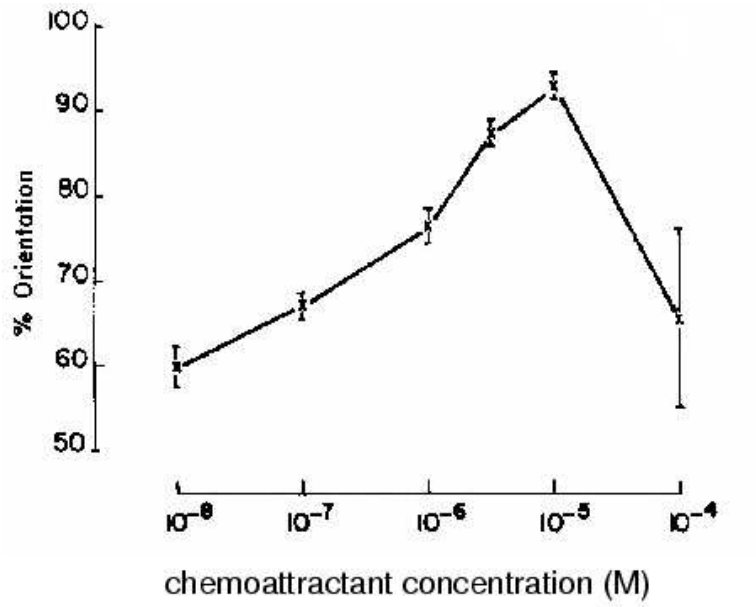

Figure 1.7: Orientation as a function of concentration of attractant. The orientation of cells exposed to a fix concentration gradient. The concentrations on the abscissa indicate the high concentration of chemoattractant present in the gradient. By Zigmond [8].

rear (like PTEN, myosin) in a gradient. However, the mechanism does not amplify external gradients at the some level of the experimental findings [21].

A two-LEGI model, where parallel mechanisms act to regulate membrane binding sites for PI3K and PTEN, which together regulate PIP_3, the main PH domain binding site was shown to increase the level of amplification in [21]. In this model, two LEGI mechanisms, acting independently in parallel, induce the complementary regulation of membrane binding/activation sites for PI3K and PTEN upon chemoattractant stimulation. Each regulator controls the number of membrane binding sites that allow for enzyme association and activation on the membrane of PI3K and PTEN, respectively. The two enzymes then catalyze the conversion between phosphatidylinositol bisphosphate PIP_2 and PIP_3. The first LEGI mechanism generates PI3K binding sites on the membrane. The molecule responsible for fast excitation (E_{PI3K}) is confined to the membrane, whereas the slower inhibitory molecule (I_{PI3K}) is allowed to diffuse freely in the cytoplasm. This mechanism results in a transient increase of PI3K binding sites in response to uniform stimulus, and an accumulation of PI3K binding sites on the side of the cell facing the

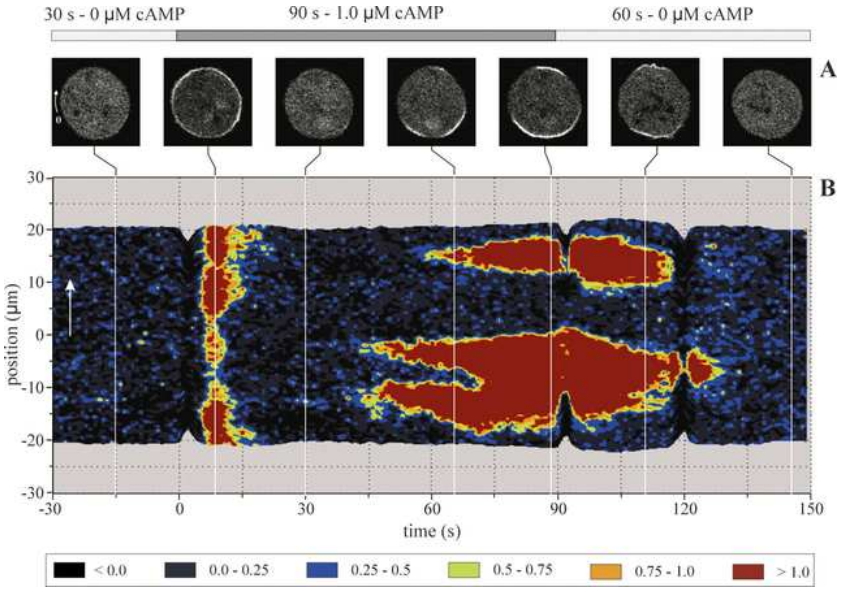

Figure 1.8: Patch formation in stimulated cell cells by cAMP. Cells were stimulated at time t=0 seconds with 1 μm cAMP and washed with buffer at t=90 seconds. (Top) The fluorescence intensity and the shape of a representative cell section before and after stimulation with cAMP. (Botton) The fluorescence intensity on the surface for the same cell. By Postma et al [15].

chemoattractant gradient. PTEN binding sites are controlled by a second LEGI mechanism using separate excitation (E_{PTEN}) and inhibition ($I_{PTEN)}$) molecules Fig.1.10. In this case, however, the response regulator destroys active binding sites. This results in a transient depletion of membrane binding sites for PTEN under uniform stimulation and a localization of binding sites for PTEN at the posterior membrane under graded inputs. The PTEN and chemoattractant concentrations are inversely correlated, and thus there was assigned a linear inhibition of PTEN binding sites. This model assumes no cross talk between the two channels of binding/activation of PI3K and PTEN.

A "balanced inactivation" model has been presented recently by Levine at al [16] to induce the switch-like behavior observed in the spatial distribution of PH domains. This model shares some of the features of the LEGI mechanism, including the receptor-mediated production of two opposing signals, one of which is local, the other global. Its innovative feature is a third component: a membrane bound inactivator that is mutually antagonistic to the response. This extra component induces a switch-like response to exter-

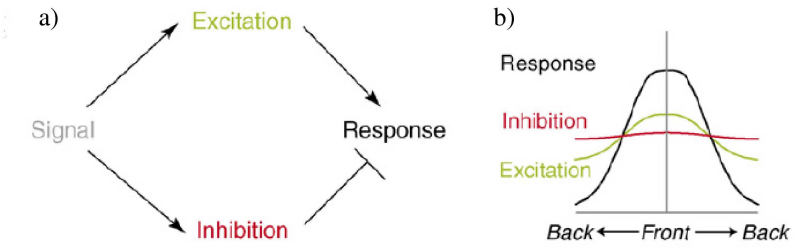

Figure 1.9: Local excitation, global inhibition model of gradient sensing. a) The premise of the model is that receptor occupancy triggers both a rapid, excitatory, local excitation as well as a slower, inhibitory, global response, which can represent the action of a diffusive inhibitor. Together, they regulate the cellular response. b) In a gradient of receptor occupancy, the excitatory signal at the front is stronger than that of the back. Though the inhibitory signal is also triggered more strongly at the front, at steady state it (mostly) equilibrates in space because of diffusion. This leaves a stronger static response at the front (where excitation exceeds inhibition) than at the rear (where inhibition exceeds excitation). By Iglesias and Devreotes [18].

nal gradients. In this model a possible candidate for the third component is a G protein which creates two complex one is ipotized to be the activator of membrane bound and another is ipotized to be the inactivator, which can diffuse in the cytoplasm. So the "balance" between activated and inactivated membrane-bounds is given by the rate of production of activator and inhibitor, originated by the some protein.

There are other hypothesized mechanisms very detailed and involves a number of additional regulatory proteins see for example [22]. The point of view of the cited model is more or less biochemicaly precise. The method is the computations of coupled equations to calculate the concentration of different species on cell membrane.

Recentely models based on physical mechanism were presented. In physical terms, the process of directional sensing shows the characteristic phenomenology of phase separation.

A first model made in this sense is the model made by Gamba et al [4]. It is a stochastic reaction-diffusion model, on a spherical lattice, the binding of PI3K to activated membrane receptors, binding of PTEN to PIP_2, catalytic activity of PI3K and PTEN, and phosphoinositide diffusion within the plasma membrane. The simulated mechanism shows that even in the absence of direct enzyme-enzyme or phosphoinositide-phosphoinositide in-

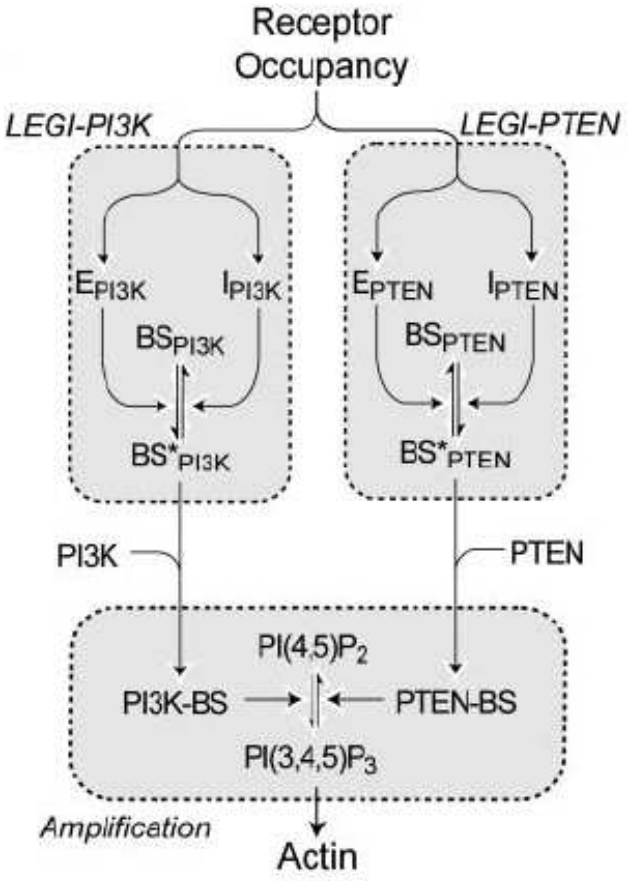

Figure 1.10: Model for regulation of PIP_3 through complementary local excitation, global inhibition (LEGI) response regulators. Receptor occupancy regulates two LEGI mechanisms working in parallel. In LEGI-PI3K, the excitation process activates more binding sites for PI3K (BS_{PI3K}/BS_{PI3K}), whereas in LEGI-PTEN, excitation destroys binding sites (BS_{PTEN}/BS_{PTEN}). Binding and activation of the enzymes follows the spatial distribution of the binding sites. Together, the two enzymes enhance the spatial resolution of PIP_3 by increasing phosphorylation of PIP_2 (by activated PI3K) and decreasing dephosphorylation of PIP_3 (by activated PTEN) at the front. By Ma et al [21].

teractions, catalysis and phosphoinositide diffusion mediate an effective interaction among enzymes, which is sufficient to drive the system toward phase separation (polarization). Particular attention in this model is dedicated to enstabilish the physical characteristic of the phenomenon; infact a description of the phase separation by an order parameter is used and there is the emergence of of phase separation region containing the concentration of activated receptors and the diffusivity of the lipids in membrane.

The idea of phase separation thogheter with the experimental observation of the formation of signaling patches [15] motivated the recent model by Gamba et al. [13]. This is a physical model which represents the eukaryotic directional sensing as a patch coalescence of phosphoinositides rich-zone, like a first order phase transition. After stimulation by chemoattractant the PIP_2-PTEN phase in unstable and there is a nucleation of PIP_3 (the stable phase) domains and subsequently a coarsening process of the largest domains which grow at the expense of smaller patches which shrink, leading to scaling lows and universal probability distribution of patch sizes.

1.5 A Statistical Mechanics approach

The statistical physics explain the emergence of complex behaviors in physical systems from simplified models of microscopic interactions and dynamical laws. It seems likely that these tools will turn more and more useful in understanding the behavior of biological systems.

In this thesis we study a Statistical Mechanics approach which capture the physical mechanism which lies behind the details of the biological process of directional sensing.

At the heart of directional sensing lies a chemical phase separation process taking place on the inner surface of the cell membrane. We inspirate to the biological mechanism presented in [4] and resumed in the cartoon showed in Fig. 1.11. It is easy to observe that from a physical point of view, there is a spatial organization phenomena which may be seen as self-organized phase ordering processes. During the process the cell state, spontaneously, or because driven by an anisotropy of an external field, decays into a state of coexistence of two chemical phases, spatially localized in different regions in order to define a front and a rear.

By making the simplest assumption that the dynamics can be derivable from free energy minimization, one would expect that the coexistence between the PI3K-rich and the PTEN-rich phase would require a fine tuning of the chemical potential difference between the two species. Phase separation takes place instead for a wide range of absolute concentration of the attrac-

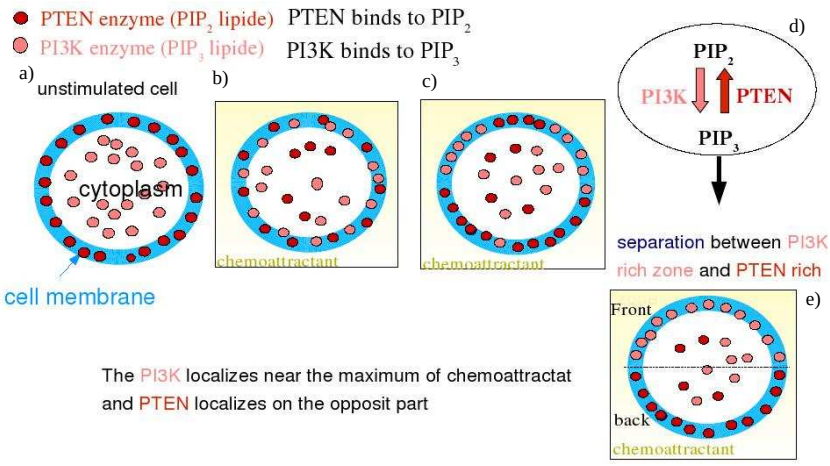

Figure 1.11: A schematic representation of directional sensing process, as is simulated by Gamba et al [4]. a) An unstimulated cell presents only PTEN on cell membrane. b) After stimulation the PI3K goes on surface and part of the PTEN goes in cytoplasm. d) e) The competing enzymatic actions of enzymes on lipids produce a segregation between enzymes an lipids of some kind.

tant, and therefore of absolute values of the chemical potential for PI3K adsorption.

In the next chapter we present a lattice-gas model based on an Hamiltonian formalism, that explains in a natural and simple way the main features of phenomenology of directional sensing [23]. The model dynamics leads from an initially unpolarized (anoriented) state to a phase separation polarized (oriented) state.

Our description is not alternative to more detailed microscopic descriptions using stochastic modeling of the relevant chemical reactions. The two descriptions are actually complementary. The microscopic description is closer to reality, but it contains several parameters whose values are not easily determined with the desired precision, and can be studied only by numerical simulations. On the other hand, a description based on Hamiltonian approach provide a more synthetic picture to describe the system and it is also amenable to an analytic study. In chapter 3 we show an analytic and numerical treatment of the directional sensing Hamiltonian in the framework of the N large model.

Chapter 2

Lattice-gas model for Eukaryotic Directional Sensing

Previous study of a stochastic reaction-diffusion model of eukaryotic polarization [4] evidenced the existence of a clear separation of timescales between faster processes, such as cytosolic diffusion and catalysis, and slower processes, such as the evolution of phase boundaries leading to phase ordering. An average over the degrees of freedom with the faster relaxation times may be performed, allowing to describe the order parameter through the use of an effective free energy [13].

We therefore considered the probabilities of enzymes to bind and unbind to the membrane, and interpreted these as obtained from a Hamiltonian formulation. Very interestingly, when the effective equivalent Hamiltonian is derived, beside the short range attraction, a long range repulsion appears as a consequence of the finiteness of the enzyme reservoir. While in presence of a pure short range attraction phases can coexist only for a definite value of the chemical potential (represented here by the external chemoattractant), the long range repulsion makes possible phase coexistence for a wide range of external chemoattractant. The simulation dynamically approaches a final polarized stationary state, with a phase coexistence of a PI3K rich and a PTEN rich domain, as experimentally observed.

2.1 The lattice model

We represent the cell membrane by a square lattice of size L with N sites, using periodic boundary conditions. The sites i occupied by PI3K (PTEN)

are described by a $S_i = +1$ (-1) spin [1]. We denote by $N^{\pm}_{\rm tot}$ the total number of ± 1 enzymes in the cell, which is given by the sum of the number of cytosolic (free) enzymes and the number of membrane-bound enzymes: $N^{\pm}_{\rm tot} = N^{\pm}_{\rm free} + N^{\pm}$.

The probability that a PI3K enzyme binds to site i is proportional to the number of cytosolic PI3Ks and to the density of binding sites (activated receptors with local concentration c_i and PIP_3's). As a first approximation, the PIP_3 concentration can be assumed to be linearly dependent from the density of PI3Ks. This gives, on site i:

$$\mathcal{P}(-1 \to +1) \propto \left[c_i + \alpha^+ \left(c_0^+ + \beta^+ \sum_{j \in \partial i} S_j \right) \right] N^+_{free} \tag{2.1}$$

where α^+, β^+, c_0^+ are functions of the chemical reaction rates, and ∂i are the nearest neighbors of i. Similarly, the probability that a PTEN molecule binds to site i is proportional to the number of free PTENs, and to the concentration of PIP_2:

$$\mathcal{P}(+1 \to -1) \propto \alpha^- \left(c_0^- - \beta^- \sum_{j \in \partial i} S_j \right) N^-_{free} \tag{2.2}$$

We interpret $\Delta\mathcal{H} = \ln[\mathcal{P}(-1 \to +1)/\mathcal{P}(+1 \to -1)]$ as an energy difference (in units of $k_B T$) between states $S_i = +1$ and $S_i = -1$, depending both on the local field $\sum_{j \in \partial i} S_j$ and on the number of cytosolic PI3Ks and PTENs.

Since $N^+ + N^- = N$, we can express N^+_{free} and N^-_{free} as functions of the magnetization $m = (N^+ - N^-)/N$. Linearizing $\Delta\mathcal{H}$ around $\sum_{j \in \partial i} S_j = 0$ and $m = 0$, we obtain:

$$\Delta\mathcal{H} = -2J \sum_{j \in \partial i} S_j - 2h_i + 2\lambda\, m \tag{2.3}$$

where $J = \frac{1}{2}\left(\frac{\alpha^+\beta^+}{c_i + \alpha^+ c_0^+} + \frac{\beta^-}{c_0^-} \right)$, $h_i = \frac{1}{2} \ln\left(1 + \frac{c_i}{\alpha^+ c_0^+}\right) - h_0$, with $h_0 = \frac{1}{2} \ln\left(\frac{\alpha^- c_0^- m^+}{\alpha^+ c_0^+ m^-} \right)$, and $\lambda = \frac{1}{2}\left(\frac{1}{m^+} + \frac{1}{m^-} \right)$, with $m^{\pm} = 2N^{\pm}_{tot}/N - 1$. If $\frac{\beta^+}{c_0^+} < \frac{\beta^-}{c_0^-}$ we can neglect the dependence of J on the attractant concentration c_i.

Eq. (2.3) corresponds to the variation of the Hamiltonian

$$\mathcal{H} = -J \sum_{\langle ij \rangle} S_i S_j - \sum_i h_i S_i + \frac{\lambda}{N} \sum_{i<j} S_i S_j. \tag{2.4}$$

[1] One can imagine performing a coarse-graining of the system on an appropriate length scale and associating a $+1$ sign to PI3K-rich sites and a -1 sign to PTEN-rich sites.

The model (2.4) contains a short-range ferromagnetic interaction representing the effective attractive interaction between enzymes, a long-range antiferromagnetic interaction which results from the finiteness of the cytosolic enzymatic reservoir, and an external site-dependent field representing the effect of the attractant. The latter depends on the concentration c_i of activated receptors, which we take proportional to the concentration of external attractant, in the form:

$$c_i = c(1 + \epsilon \sin^2 \frac{\pi x_i}{L} \sin \frac{2\pi y_i}{L}), \tag{2.5}$$

where ϵ is a percentage of anisotropy. We use the form 2.5 to respect the periodic boundary conditions.

When h_i is independent of i, the second and third term of Eq. (2.4) can be written (apart from a constant) as $\frac{N\lambda}{2}(\frac{h}{\lambda} - m)^2$, so that energy minimization leads the system to self-tune to the magnetization value h/λ. Eq. (2.3) shows that S_i is subject to the action of an effective external field $h_{\mathrm{eff},i} = h_i - \lambda\, m$. The value $h_{\mathrm{eff},i}$ measures the degree of metastability of the PTEN phase, and tends to zero during the self-tuning evolution of the system.

Beside the external attractant concentration, the model depends on four independent parameters, J, h_0, λ and $\alpha^+ c_0^+$. These parameters are functions of the biological parameters, like molecule concentrations or reaction rates. We chose the units for the external attractant concentration so that $\alpha^+ c_0^+ = 1$. To realize phase separation, J has to be larger than the critical value for the two-dimensional Ising spin model ($J \simeq 0.44$), here we set $J = 1$. h_0 measures the relative affinity of PTEN enzymes to the cell membrane with respect to PI3K enzymes, in the absence of external attractant. The unstimulated cell membrane is entirely occupied by PTEN, implying $h_0 \geq 1$, we set here $h_0 = 1$. Finally, λ measures the relative abundance of the two type of enzymes in the cell, we set here $\lambda = 1$.

2.2 Simulations

We study by Monte Carlo simulations the dynamics and the final state attained by the system, using a square lattice of size $L = 2048$. For each step we select a lattice site randomly and we estimate the probability for spin reversal as follows:

$$P = \begin{cases} 1 \quad if \quad \Delta H \leq 0 \\ \\ exp(-\Delta H) \quad if \quad \Delta H > 0 \end{cases} \tag{2.6}$$

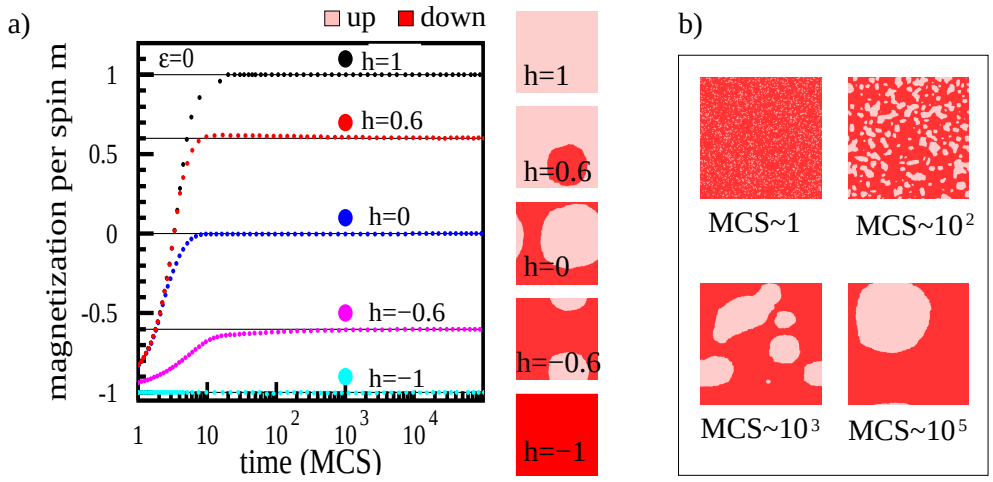

Figure 2.1: a) Self-tuning dynamics in the presence of a uniform activation field h. The magnetization m grows to compensate the external activation field h. On the right, equilibrium states corresponding to different values of h. b) Coarsening dynamics leading to random membrane polarization in the presence a uniform activation field.

We first consider the case $\epsilon = 0$, which corresponds to uniform stimulation. In the absence of stimulation ($c = 0$, implying $h = -1$ and $m = -1$) the membrane is uniformly populated by PTEN molecules. Setting $c > 0$ (which implies $h > -1$), spin up (PI3K) domain nucleation is started in the spin down (PTEN) sea. The magnetization m tends asymptotically to h, while the effective field h_{eff} tends to zero (Fig. 2.1a), realizing the condition for phase coexistence. The unit of time is Monte Carlo steps (MCS). The correspondence between MC steps and physical time is not straightforward. We imposed detailed balance, that regards the ratio between transition probabilities, while physical time depends on the absolute value of those probabilities. Anyway, one MC step corresponds to the time in which there is a probability of order one to bind or unbind one enzyme on each site. One MCS has to be identified with the characteristic binding/unbinding time for one enzyme. Using realistic values for association/dissociation constants [4] this gives 1 MCS$\sim$ 0.01 seconds.

After a rapid nucleation phase, a domain coarsening dynamics follows: large domains grow and smaller ones shrink [9] (Fig. 2.1b). The final equilibrium state is characterized by the coexistence of the PI3K and the PTEN phase, localized in two complementary clusters. The equilibrium position of the PI3K cluster, which determines the direction of cell movement, is ran-

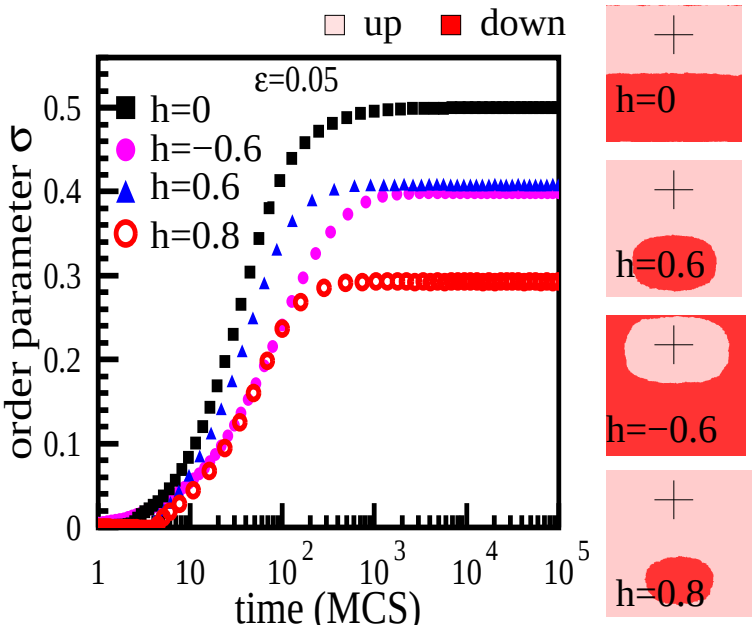

Figure 2.2: Time evolution of the order parameter for different values of the activation field h, and for a fixed value $\epsilon = 0.05$ of the gradient. At the end of the polarization process the PI3K cluster (gray in the panels on the right) is centered around the point of maximum attractant stimulation (crosses).

dom. This behavior is consistent with experiments in which cells exposed to a uniform attractant distribution orient randomly (stochastic polarization) [8].

In the presence of a gradient in the chemical attractant ($\epsilon > 0$) the PI3K cluster localizes around the maximum of the attractant density. To measure the polarization degree we define the following order parameter:

$$\sigma = \frac{1}{2}\frac{\sum_i^N (c_i - c)S_i}{\sum_i^N |c_i - c|}, \tag{2.7}$$

which is both a measure of the degree of order in the system and of the correlation of the center of the PI3K cluster with the maximum of the attractant density (Fig. 2.2).

2.2.1 Dose-response curve

Simulations reproduce the qualitative behavior of experimentally observed dose-response curves [10, 8], showing no response for either very high or very low values of the attractant concentration, optimal response for several

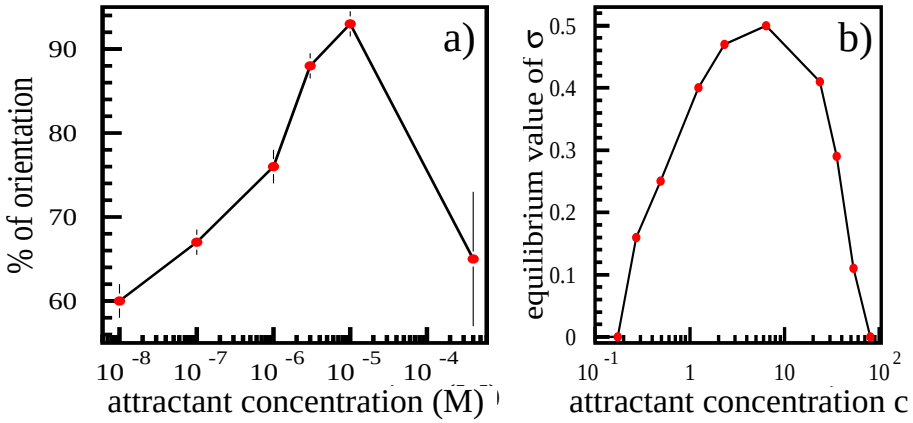

Figure 2.3: a): Orientation degree of a population of cells as a function of the attractant concentration, for a constant gradient (adapted from [8]). b): Simulated equilibrium values of the order parameter σ as a function of the attractant concentration c, for a constant gradient. A null value of the order parameter (no polarization) corresponds to random movement of real cells (50% of cells directed towards higher chemotactic concentration). Units in b) are arbitrary. A realistic scale is obtained by observing that saturation for high values of c corresponds to uniform +1 configurations, *i.e.* to receptor saturation in real cells.

decades of intermediate values (Fig. 2.3). This effect can be explained as follows. For very low c the critical radius for patch nucleation is larger than the size of the cell, and no polarization is possible. For very high c, such that $h > 1$, the equilibrium magnetization is 1, the whole system is uniformly populated by the PI3K phase, and again no polarization is possible. Polarization is possible only for values which are intermediate between these two limit cases.

2.2.2 Reversibility

Polarization induced by the gradient is reversible. By changing the gradient direction after the system has reached equilibrium, the position of the PI3K cluster adjusts to the new direction in a finite time 2.4. This effect reproduces the observed reorientation of eukaryotic cells under varying attractant gradients observed in the experiments [11]. Interestingly, after changing the sign of the relative gradient we observed reorientation taking place by a collective movement of the PI3K cluster, and not by its evaporation and successive

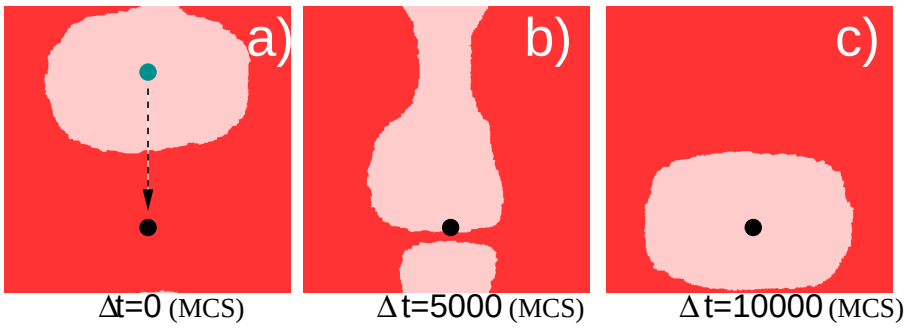

Figure 2.4: Sequence of immage of the system after the inversion of gradient. The position of the maximum of the chemoattractant concentration is marked by the circle.

recombination.

2.2.3 Gradient amplification and polarization time

The transient states are characterized by a coarsening dynamics with the appearance of scaling laws in the process of domain formation [9, 13, 12]. Our simulations show that, for a condition of uniform distribution of attractant, in the initial coarsening stage the average cluster radius $\langle r \rangle$ grows approximately as $t^{1/2}$. In Fig. 2.5a the inverse length of the total cluster boundary is plotted against time [2]. We define the polarization time $t_{\rm p}$ as the time for which the order parameter σ reaches 90% of its equilibrium value. If the attractant is uniformly distributed the coarsening process stops when the average cluster radius becomes of the order of the cell size, $r \sim L$, implying that the spontaneous cell polarization time scales as $t_{\rm p} \sim 1/L^2$.

In the case of an attractant gradient we observe instead a double scaling behavior. For $t < t_\epsilon$, where t_ϵ is a crossover time depending on the amplitude of the gradient ϵ, cluster growth proceeds approximately as in the uniform case, while, for $t > t_\epsilon$, the process of polarization becomes anisotropic, and the average cluster size grows approximately linearly in t (Fig. 2.5a). The presence of this double scaling law implies that the polarization time behaves as $t_{\rm p} \sim a + b/\epsilon + c/\epsilon^2$ (Fig. 2.5b). We can understand the double scaling law as follows. In the presence of an attractant gradient polarization takes place in two steps. In the initial (tuning) step the gradient of the attractant is negligible with respect to the uniform component of the attractant and

[2] If the system is composed of circular domains, the inverse length of the total cluster boundary scales as the mean radius of the clusters.

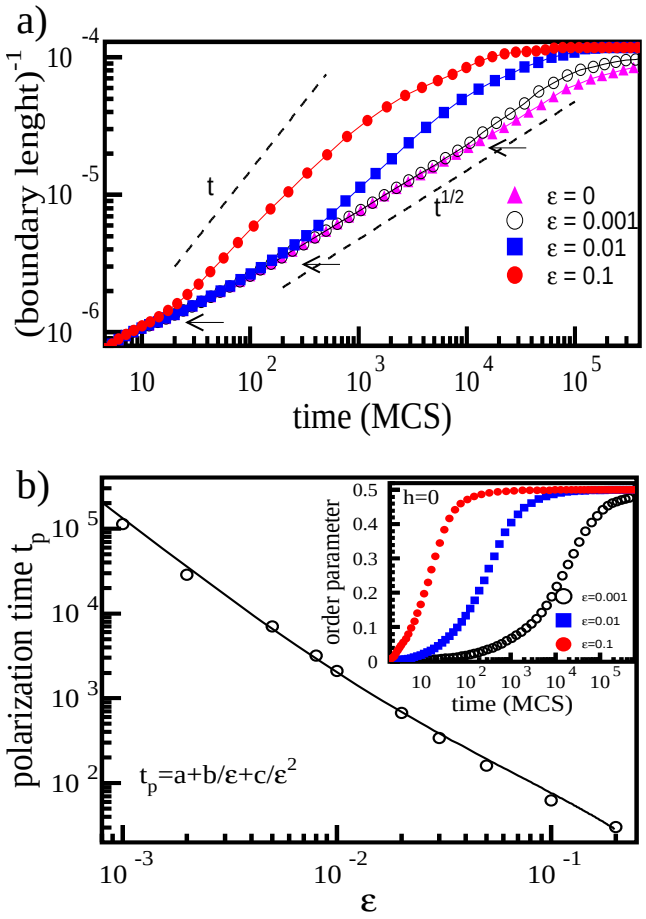

Figure 2.5: a) Time evolution of the inverse length of the total cluster boundary for different values of the gradient ϵ. The dotted lines show the slope of the power-law behaviors characterizing the growth regimes dominated, respectively, by the uniform component of the attractant ($\sim t^{1/2}$) and by the gradient ($\sim t$). Arrows show the position of crossovers between the two scaling behaviors. b) Polarization time as a function of ϵ, and time evolution of the order parameter σ for different values of ϵ (inset).

cluster growth is approximately unaffected by its presence. Meanwhile, free enzymes shuttle from the cytosolic reservoir to the membrane, lowering the chemical potential for further cluster growth and effectively canceling out the effect of the uniform component of the attractant. This process continues until times of order t_ϵ, when only the effect of the gradient component is left. At this point, fast polarization in the direction of the gradient takes place. The anisotropic stage of cluster evolution leading to directed polarization occurs only if $t_\epsilon < t_{\rm p}$. Otherwise, the presence of a gradient of attractant becomes irrelevant and only the stage of isotropic patch growth actually occurs. The crossover time t_ϵ increases with decreasing ϵ until it becomes of the order of $t_{\rm p}$, implying the existence of a lower threshold $\epsilon_{\rm th}$ of detectable gradients. For $\epsilon > \epsilon_{\rm th}$ anisotropy-induced polarization is much faster than spontaneous polarization. This explains the experimentally observed effect of gradient amplification in chemotacting cells and the observation [10] of a lower threshold of detectable gradients, below which there is no directional sensing. These results also confirm the theoretical predictions of [13].

2.3 Discussion

We have introduced a simple lattice-gas model describing the process of eukaryotic directional sensing. Analysis of this model via Monte Carlo simulations shows that it reproduces important aspects of the observed phenomenology and sheds light on the underlying physical mechanism. The model maps signaling molecules and enzymes in spin variables, and the effective interaction between enzymes on the membrane into a ferromagnetic coupling. Enzymes shuttling from the cytosolic reservoir to the membrane is shown to provide a fundamental self-tuning mechanism which drives the system towards phase coexistence and polarization, by counteracting the effect of the external activation field. In the presence of an attractant gradient this mechanism cancels out the isotropic component of the attractant distribution in a first (tuning) stage of cluster growth, preparing the ground for fast directed polarization in the direction of the gradient in the next stage. The control provided by enzyme shuttling is encoded in the coupling of the effective magnetic field $h_{\rm eff}$ with the local order parameter m, thus realizing an effective long-range repulsion between enzymes and introducing in the model an element of self-organization. The existence of two distinct stages in cluster evolution when an attractant gradient is present is signaled in the model simulations by the emergence of a double power law for the time evolution of clusters of signaling molecules. This shows up in the dependence of directed polarization time from the gradient: for $\epsilon \ll 1$, t_ϵ scales as ϵ^{-2}.

We have shown that the phenomenology of eukaryotic directional sensing, including gradient amplification and independence on the absolute value of the stimulation, may be understood as the result of the peculiar growth dynamics of clusters of stable chemical phases induced by nonlinearities in the underlying biochemical network, coherently with previous results [13, 4]. Our approach leads to the prediction of new observable effects, such as the scaling behavior of polarization times as a function of applied gradients. Our results are mostly independent on the details of the underlying reaction network, although they were inspired by the particular biochemical mechanism described in [4]. In a number of recent papers [16, 17] (see also [18] for a comprehensive review) similar mechanisms, based on the competition of an activatory and an inhibitory channel, have been proposed. As long as the nonlinearities contained in the corresponding reaction networks allow for the formation on the cell membrane of chemically distinct phases, and the intrinsic stochasticity of the cellular environment is taken into account, our analysis should apply with minimal modifications to these models as well.

Chapter 3

Large N model for Eukaryotic Directional Sensing Hamiltonian

In complex systems there are various mechanisms that give rise to organization and pattern formation. In the living organisms the pattern formation of two or more substances determines a symmetry breaking which allows the orientation. In particular the Eukaryotic cells are able to sense and adapt to external chemicals signals. During the directional sensing a cell transduces and amplifies the external chemical signal in an internal distribution of signaling molecules: two enzymes or lipids which localize in opposite part of cell surface. From a physical point of view, these spatial organization phenomena may be seen as self-organized phase ordering processes, where the cell state, spontaneously, or driven by an anisotropic external field, decays into a state of coexistence of two or more chemical phases, spatially localized in different regions in order to define a front and a rear.

In the previous chapter we gave a physical interpretation of eukaryotic directional sensing as a phase separation of two components. We showed a treatment of this phenomenon using a Hamiltonian approach. The biological process was modeled by a pattern formation in a binary spin system regulated by Glauber dynamic.

In this chapter, inspirated by the mechanism of eukaryotic directional sensing, we present a treatment of system with competing short-range attraction and long-range repulsion using a Ginzburg-Landau functional in the limit of infinite order parameter dimension N [28],[27].

We derive a phase diagram in function of the external field and the intensity of the long-range repulsion, which delimits the region of parameters where the phase coexistence and separation is possible.

We also derive time dependent motion equations in the scheme of non-conserved order parameter and study the time dependent behavior of magnetization and correlation function.

In the next paragraphs we introduce the field theories and the large N limit, then we treat the model 2.4 in the case of uniform external field first and after in the case of non-uniform external field.

3.1 Field theory

The Ginzburg-Landau model has its origin in the Landau mean field theory. The mean fields theories are widely used to reduce the mathematic complications and find many qualitative and quantitative results. Landau theory is remarkable in that, under the simple assumptions that the order parameter is small near T_c, it yields a wealth of informations about phase transitions.

Landau gave a phenomenological expansion of the free energy f in powers of the order parameter m (the density of magnetization for example). Supposing that f is analytic function, it is possible to arrest at 4th order in m. The temperature can be included in the coefficients of the expansion. For the Ising ferromagnet the free energy must be invariant under time reversal. Since m changes sign under time reversal, f must be invariant under $m \to -m$, i.e. only even powers of m are permitted in the expansion. Then f assume the following form:

$$f = a(T)m^2 + b(T)m^4. \tag{3.1}$$

Assuming that $a(T)$ becomes zero for a certain Temperature called critical T_c and $a(T)$ and $b(T)$ are analytic near T_c, at lowest order $a(T) \sim a_0(T - T_c)$ and $b(T) \sim b_0$. The free energy (3.1) has two minima for $T < T_c$ and one for $T > T_c$ [25]. The form (3.1) of free energy is sufficient to take in account the spontaneous magnetization in the phase transition of Ising model.

In order to treat also the role of fluctuations it is often more useful to introduce semi-phenomenological field theories, all points on a lattice of local order parameter treated as a continuous classical fields $\phi(x)$. It is also convenient to set up the description of a system in terms of Landau free energy functional.

The continuum limit of a lattice model is obtained by allowing the volume for lattice site v_0 to tend to zero, the coordinates of the site i become a continuous variable $\vec{x}$, and the spin variable S_i to become a field $\phi(\vec{x})$ while keeping the total volume $V = nV_0$ constant (n is the spin number)[26]. In

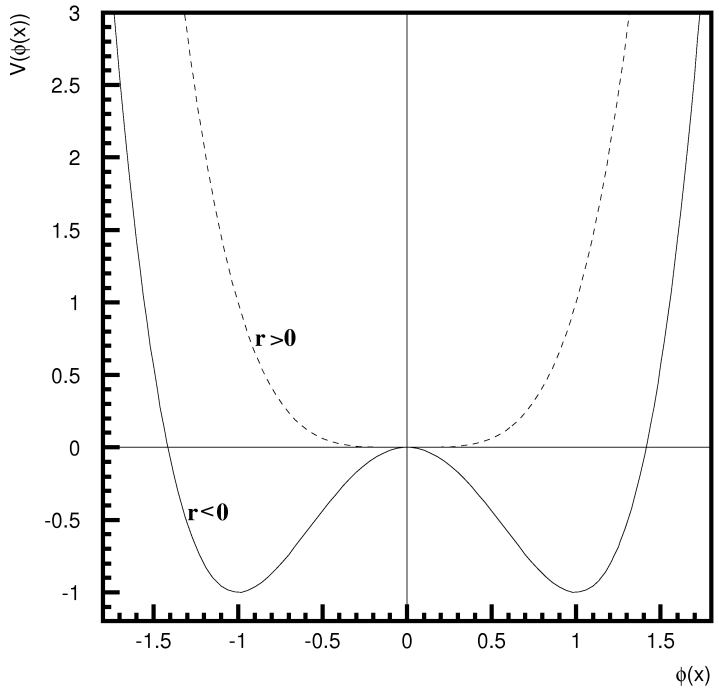

Figure 3.1: Typical form of the symmetric double-well potential $V(\phi(x))$.

this limit

$$v_0 \sum_i = \int_V d^d x \tag{3.2}$$

The total free energy will be:

$$\begin{aligned} F &= \int d^d x \frac{1}{2} (\nabla \phi(x))^2 + V(\phi(x)) = \\ &\int d^d x \frac{1}{2} (\nabla \phi(x))^2 + r\phi^2(x) + g\phi^4(x), \end{aligned} \tag{3.3}$$

Where $r \propto T - T_c$ and $g > 0$. $V(\phi(x))$ has a double-well structure of Fig. 3.1, the two minima of V correspond to $r < 0$ and they are the two equilibrium states, while the gradient-squared term in (3.3) associates an energy cost to an interface between the phases.

3.1.1 Dynamical models

When a system in high temperature is quenched to a temperature below its ordering temperature it orders kinetically. A long-wavelength instability amplifies the fluctuations in the initial state leading to the formations of domains of macroscopic size. At late time, phase separating systems are usually characterized by a single time dependent length, the average domains size $L(t)$, which grows as a power low $L(t) \sim t^z$. The growth exponent z is a characteristic of the mechanism driving the phase separation. Trough it, phase separating systems may be classified into a small number of universality classes, where each member of a given class shares the same kinetic properties. These universality classes depend crucially upon the presence or absence of conservation laws. The ordering systems exhibit scaling behavior characterized by the growing exponent z. In fact the scaling hypothesis states that the domain structure is independent of time when lengths are scaled by the characteristic length $L(t)$[27]. In terms of the structure factor (Fourier transform of the equal time order parameter correlation function) the asymptotic scaling behavior is of the form

$$C(k,t) \sim L^a(t) F(kL(t)), \tag{3.4}$$

where $F(kL(t))$ is a scaling function and a is the growing exponent $a \sim z$ for the late stage. There are two main universality class of system in the process of phase ordering, characterized by dynamic [12] of the order parameter.

In the case where the order parameter is not conserved, the appropriate equation for time evolution of the field $\phi(x)$ is given by the variation of the free energy functional respect the field:

$$\frac{\partial \phi(x)}{\partial t} = -\frac{\delta F}{\delta \phi(x)}, \tag{3.5}$$

this kind of equation is called Time-Dependent-Ginzburg-Landau (TDGL) equation. This dynamic correspond in the spin language to the single spin flip called also Glauber dynamic. For a system with scalar order parameter driven by (3.5) the growth is curvature driven with $z = \frac{1}{2}$.

When the order parameter is conserved as in the spinodal decomposition, there is another dynamic. It requires the local conservation of the value of the field $\phi(x)$:

$$\frac{\partial \phi(x)}{\partial t} = -\nabla^2 \frac{\delta F}{\delta \phi(x)}, \tag{3.6}$$

which has the form of a continuity equation, $\partial_t \phi(x) = -\nabla \cdot j$, with the current $j = -\nabla \delta F / \delta \phi(x)$. The equation 3.6 is called Cahn-Illiard equation, which

correspond in the spin language to the Kawasaky dynamic, which requires, for a spin flip, the flipping of one of its first neighbors. A kind of dynamic (3.6) gives $z = \frac{1}{3}$.

In the present thesis we focus on the non conserved order parameter scheme.

3.2 Large N model

In the study of critical phenomena there are mathematical complication for the large and strong fluctuation in the order parameter. When you consider not any more a scalar field $\phi(x)$ but an N component vectorial field $\vec{\phi}(x)$ in the space of the order parameter, the fluctuation of the magnitude of the N-component field vectors is small. Even if each component may fluctuate a lot, the sum of the squares N field components is a large number and it is fixed at its average value apart small fluctuations of the order of $1/\sqrt{N}$. In the limit $N \to \infty$ the approximation becomes exact [28].

It is always possible, for example using a form (3.3) for the the free energy, to write the equilibrium probability distribution function of the order parameter in the form:

$$P \propto e^{-F[\vec{\phi}(x)]} \tag{3.7}$$

and the physical interesting quantity which are the average values will be:

$$\langle A \rangle = \frac{\int D\vec{\phi}(x)\, A e^{-F[\vec{\phi}(x)]}}{\int D\vec{\phi}(x)\, e^{-F[\vec{\phi}(x)]}}. \tag{3.8}$$

The integration $\int D\vec{\phi}(x)$ is on all the possible field configuration. If the 4th power of ϕ term of (3.3) is absent, then P would be a Gaussian and the calculation of quantities (3.8) would be simple. The presence of ϕ^4 term makes the calculation very difficult. The problem simplify when N is large. When $N \to \infty$, the $\vec{\phi}^4$ term can be written as:

$$\vec{\phi}^4 = (\vec{\phi}^2)^2 = \langle \vec{\phi}^2 \rangle \vec{\phi}^2 \tag{3.9}$$

So the the free energy functional is:

$$F[\vec{\phi}(x)] = \int d^d x \frac{1}{2} (\nabla \vec{\phi}(x))^2 + (r + g\langle \vec{\phi}^2 \rangle) \vec{\phi}^2(x)). \tag{3.10}$$

By Fourier transform:

$$F[\vec{\phi}(k)] = \frac{1}{2} \sum_{\alpha, k<\Lambda} (k^2 + r + g\langle \vec{\phi}^2 \rangle) \vec{\phi}^2_\alpha(k)), \tag{3.11}$$

where α is the generic component of the field $\vec{\phi}$ in the order parameter space, Λ is a cut-off on wave vector and k is the modulus of the wave vector. The remarkable fact is that $\langle\vec{\phi}^2\rangle$ is a constant and will not affect the average values calculated via $P \propto e^{-F[\vec{\phi}(k)]}$. The probability is thus a product of Gaussians, one for each component of the field (α, k) and the average of $\langle\vec{\phi}^2\rangle$ is:

$$\langle\vec{\phi}^2\rangle = L^{-d} \sum_{\alpha,k<\Lambda} \langle\phi_\alpha(k)^2\rangle. \tag{3.12}$$

As we understood in the previous paragraph, a very important quantity for the dynamical properties of a system is the equal time correlation function $C(k) = \langle\phi_\alpha(k)^2\rangle$ giving:

$$C(k) \;=\; (k^2 + r + g\langle\vec{\phi}^2\rangle)^{-1}, \tag{3.13}$$

being the quantity $k^2 + r + g\langle\vec{\phi}^2\rangle$ the inverse of variance of the gaussian's product given by the probability expression. The quantity $r + g\langle\vec{\phi}^2\rangle$ is the inverse of the square of the correlation length of the system. Substituting the (3.13) in the (3.12) we find:

$$\begin{aligned}\langle\vec{\phi}^2\rangle &= L^{-d} \sum_{\alpha,k<\Lambda} (k^2 + r + g\langle\vec{\phi}^2\rangle)^{-1} \\ &= K_d \int_0^\Lambda k^{d-1}(k^2 + r + g\langle\vec{\phi}^2\rangle)^{-1}\end{aligned} \tag{3.14}$$

where K_d is the solid angle in d dimension, which cames from the integration in spherical coordinates. The (3.14) give an self-consistence relation winch has to be respected in each calculation after the $N \to \infty$ limit.

The next part is dedicated to the treatment of a free energy functional associated to the discrete Hamiltonian (2.4). It contains a short-range attraction, a long-range repulsion and an interaction with an external magnetic field.

3.3 Large N model for a system with competition between short-range attraction and long-range repulsion

The competition between a short-range attraction and a long-range repulsion together with the influence of an external magnetic field can reproduce a very

remarkable physical feature of the phenomenon of directional sensing: phase coexistence for wide range of amplitude of an external field.

We study the system using a Hamiltonian model based on Ginzburg-Landau functional in the framework of $N \to \infty$ limit.

We examine first the case of uniform external field first, which correspond to the presence of uniform chemoattractant. In this case we obtain the analytical form for the critical temperature, the behavior of magnetization and correlation function.

In the next chapter we derived the motion equation the case of an anisotropic external field which correspond to introduce a gradient in chemoattractant.

3.4 Equations of the motion for uniform h

The model 2.4 can be represented in a continuous formalism by the following free energy:

$$\begin{aligned} \mathcal{H}[\vec{\phi}] &= \int_V d\vec{x} \left\{ \frac{1}{2}(\nabla\vec{\phi})^2 + \frac{r}{2}(\vec{\phi}\cdot\vec{\phi}) + \frac{g}{4N}(\vec{\phi}\cdot\vec{\phi})^2 - \vec{H}(\vec{x})\cdot\vec{\phi}(\vec{x}) \right\} \\ &+ \frac{1}{2}\frac{\lambda}{V}\left[\int_V d\vec{x}\,\vec{\phi}\right]^2 \end{aligned} \tag{3.15}$$

where $\vec{\phi} = (\phi_1, \phi_2, ..., \phi_N)$ is the vectorial order parameter and it represents, in the scalar limit, the difference of concentration of two substances. $r < 0$, $g > 0$, $|\vec{H}(\vec{x})| \sim \mathcal{O}(N^{1/2})$ and V is the volume of the system. The long-range term $\lambda > 0$ is a ferromagnetic term.

We consider the static and dynamic properties of the model for a uniform magnetic field. Adopting the dynamical model based on the Langevin equation

$$\frac{\partial\vec{\phi}(\vec{x},t)}{\partial t} = -\frac{\delta\mathcal{H}[\vec{\phi}]}{\delta\vec{\phi}}(\vec{x},t) + \vec{\eta}(\vec{x},t) \tag{3.16}$$

where $\vec{\eta}(\vec{x},t)$ is the white noise at temperature T, with zero average and correlator

$$\langle \eta_\alpha(\vec{x},t)\eta_\beta(\vec{x}',t')\rangle = 2T\delta_{\alpha\beta}\delta(\vec{x}-\vec{x}')\delta(t-t')$$

the equation of motion of the order parameter is given by

$$\begin{aligned} \frac{\partial\vec{\phi}(\vec{x},t)}{\partial t} &= -\left[-\nabla^2\vec{\phi}(\vec{x},t) + r\,\vec{\phi}(\vec{x},t) + \frac{g}{N}(\vec{\phi}\cdot\vec{\phi})\vec{\phi}(\vec{x},t) - \vec{H}(\vec{x})\right] \\ &- \frac{\lambda}{V}\int_V d\vec{x}\,\vec{\phi}(\vec{x},t) + \vec{\eta}(\vec{x},t). \end{aligned} \tag{3.17}$$

This equation must be complemented by an initial condition, in the form of a probability distribution $P[\vec{\phi}(\vec{x},t_0)]$ of the order parameter configurations at the time t_0. It is convenient to decompose the order parameter into the sum of components longitudinal and transverse with respect to the external field $\vec{H}(\vec{x})$

$$\vec{\phi} = \vec{\phi}_{\parallel} + \vec{\phi}_{\perp} \tag{3.18}$$

and to split the longitudinal component into the sum

$$\vec{\phi}_{\parallel}(\vec{x},t) = \vec{M}(\vec{x},t) + \vec{\psi}(\vec{x},t) \tag{3.19}$$

where $\vec{M}(\vec{x},t) = \langle \vec{\phi}_{\parallel}(\vec{x},t) \rangle$ is the magnetization and the average longitudinal fluctuations vanish $\langle \vec{\psi}(\vec{x},t) \rangle \equiv 0$ by construction.

Inserting Eqs. (3.18) and (3.19) into Eq (3.17), two separate equations for the longitudinal and transverse components are obtained. Rotating the 1-axis in the order parameter space along the longitudinal direction, the first one reads

$$\begin{aligned} \frac{\partial (M+\psi)}{\partial t} &= -\Big[-\nabla^2 M + rM + \frac{g}{N} M^3 \\ &+ \frac{g}{N} (\vec{\phi}_{\perp} \cdot \vec{\phi}_{\perp}) M - (h - \lambda \overline{M}) \\ &- \nabla^2 \psi + \Big(r + \frac{3g}{N} M^2 + \frac{g}{N} (\vec{\phi}_{\perp} \cdot \vec{\phi}_{\perp}) \Big) \psi \\ &+ \frac{3g}{N} M \psi^2 + \frac{g}{N} \psi^3 + \frac{\lambda}{V} \int_V d\vec{x}\, \psi \Big] + \eta_{\parallel} \end{aligned} \tag{3.20}$$

where

$$\overline{M} = \frac{1}{V} \int_V d\vec{x}\, M. \tag{3.21}$$

Assuming, next, $M \sim \mathcal{O}(N^{1/2})$ and $\psi \sim \mathcal{O}(1)$ and comparing terms of the same order of magnitude, we obtain

$$\frac{\partial m}{\partial t} = -\Big[-\nabla^2 + r + g m^2 + \frac{g}{N} (\vec{\phi}_{\perp} \cdot \vec{\phi}_{\perp}) \Big] m + (h - \lambda \overline{m}) \tag{3.22}$$

at order $\mathcal{O}(N^{1/2})$, while at order $\mathcal{O}(1)$

$$\frac{\partial \psi}{\partial t} = -\left[-\nabla^2 \psi + \left(r + 3g m^2 + \frac{g}{N} \left(\vec{\phi}_{\perp} \cdot \vec{\phi}_{\perp} \right) \right) \psi + \frac{\lambda}{V} \int_V d\vec{x}\, \psi \right] + \eta_{\parallel} \tag{3.23}$$

where we have introduced the rescaled quantities

$$m(\vec{x},t) = M(\vec{x},t)/N^{1/2}, \;\; h(\vec{x},t) = H(\vec{x},t)/N^{1/2}. \tag{3.24}$$

The remaining contributions along the transverse directions give

$$\begin{aligned}\frac{\partial\vec{\phi}_\perp}{\partial t} &= -\Big[-\nabla^2\vec{\phi}_\perp + r\vec{\phi}_\perp + \frac{g}{N}\left(M^2+2M\psi+\psi^2\right)\vec{\phi}_\perp \\ &+ \frac{g}{N}\left(\vec{\phi}_\perp\cdot\vec{\phi}_\perp\right)\vec{\phi}_\perp + \frac{\lambda}{V}\int_V d\vec{x}\,\vec{\phi}_\perp\Big] + \vec{\eta}_\perp\end{aligned} \tag{3.25}$$

which, retaining only the $\mathcal{O}(1)$ dominant terms, becomes

$$\begin{aligned}\frac{\partial\vec{\phi}_\perp}{\partial t} &= -\Big[-\nabla^2\vec{\phi}_\perp + \Big(r+gm^2\Big)\vec{\phi}_\perp \\ &+ \frac{g}{N}\left(\vec{\phi}_\perp\cdot\vec{\phi}_\perp\right)\vec{\phi}_\perp + \frac{\lambda}{V}\int_V d\vec{x}\,\vec{\phi}_\perp\Big] + \vec{\eta}_\perp.\end{aligned} \tag{3.26}$$

Taking the large N limit

$$\lim_{N\to\infty}\frac{1}{N}(\vec{\phi}_\perp\cdot\vec{\phi}_\perp) = S(\vec{x},t) = \frac{1}{N}\langle\vec{\phi}_\perp\cdot\vec{\phi}_\perp\rangle \tag{3.27}$$

where the angular brackets denote the average over both the initial condition and the thermal noise, Eqs. (3.22), (3.23) and (3.26) become

$$\frac{\partial m}{\partial t} = -\left[-\nabla^2 + r + gm^2 + gS\right]m + (h-\lambda\overline{m}) \tag{3.28}$$

$$\frac{\partial\psi}{\partial t} = -\left[\Big(-\nabla^2 + r + 3gm^2 + gS\Big)\psi + \frac{\lambda}{V}\int_V d\vec{x}\,\psi\right] + \eta_\parallel \tag{3.29}$$

and

$$\frac{\partial\vec{\phi}_\perp}{\partial t} = -\left[\Big(-\nabla^2 + r + gm^2 + gS\Big)\vec{\phi}_\perp + \frac{\lambda}{V}\int_V d\vec{x}\,\vec{\phi}_\perp\right] + \vec{\eta}_\perp. \tag{3.30}$$

In the last equation the components of $\vec{\phi}_\perp$ are decoupled. Hence, from now on we shall refer to the equation for the generic component.

If the initial condition yields spaced translation invariant averages and the external field h is uniform, space translation invariance holds also for all subsequent times. Fourier transforming with respect to space, Eqs. (3.28), (3.29) and (3.30) become

$$\frac{\partial m(t)}{\partial t} = -\omega(0,t)m(t) + h \tag{3.31}$$

$$\frac{\partial\psi(\vec{k},t)}{\partial t} = -\left[\omega(k,t) + 2gm^2\right]\psi(\vec{k},t) + \eta(\vec{k},t) \tag{3.32}$$

$$\frac{\partial\phi(\vec{k},t)}{\partial t} = -\omega(k,t)\phi(\vec{k},t) + \eta(\vec{k},t) \tag{3.33}$$

where $\phi(\vec{k},t)$ and $\eta(\vec{k},t)$ are the generic components of $\vec{\phi}_\perp(\vec{k},t)$ and $\vec{\eta}(\vec{k},t)$,

$$\omega(k,t) = k^2 + 2\lambda\delta_{k,0} + r + g(m^2 + S) \tag{3.34}$$

and the noise correlator in Fourier space is given by

$$\langle\eta(\vec{k},t)\eta(\vec{k}',t')\rangle = 2TV\delta_{\vec{k}+\vec{k}',0}\delta(t-t').$$

With periodic boundary conditions, the allowed wavevectors are given by

$$\vec{k} = \frac{2\pi}{L}\vec{n} \tag{3.35}$$

where $\vec{n}$ is a vector with integer components and $L^d = V$. Furthermore, sums over $\vec{k}$ are cutoff to the upper value $k_{max} = \Lambda$, where Λ^-1 is related to a characteristic microscopic length, for instance the lattice spacing of underling lattice.

Using the definition (3.27) of $S(t)$ and introducing the transverse correlation function

$$\langle\phi(\vec{k},t)\phi(\vec{k}',t)\rangle = C_\perp(\vec{k},t)V\delta_{\vec{k}+\vec{k}',0} \tag{3.36}$$

a closed set of equations can be obtained

$$\frac{\partial m(t)}{\partial t} = -\omega(0,t)m(t) + h \tag{3.37}$$

$$\frac{\partial C_\perp(\vec{k},t)}{\partial t} = -2\omega(k,t)C_\perp(\vec{k},t) + 2T \tag{3.38}$$

$$S(t) = \frac{1}{V}\sum_{\vec{k}} C_\perp(\vec{k},t) \tag{3.39}$$

with $\omega(k,t)$ defined in Eq. (3.34). The longitudinal fluctuations do not enter the self-consistency relation and remain determined either by Eq. (3.32), or by

$$\frac{\partial C_\parallel(\vec{k},t)}{\partial t} = -2\left[\omega(k,t) + (2g/N)m^2(t)\right]C_\parallel(\vec{k},t) + 2T \tag{3.40}$$

where $C_\parallel(\vec{k},t) = \langle\psi(\vec{k},t)\psi(-\vec{k},t)\rangle$.

Since the longitudinal structure factor is completely determined, from now on shall concentrate on the tree coupled equations (3.37), (3.38) and (3.39).

3.4.1 Static properties

Let us now analyze the final equilibrium states. In the limit $t \to \infty$ the left hand side of Eqs. (3.37), (3.38) and (3.39).

If equilibrium is reached, all quantities become time independent. Rewriting Eq. (3.34) as

$$\omega(k) = \begin{cases} \lambda + \mu, & \text{for} \quad k = 0 \\ k^2 + \mu, & \text{for} \quad k \neq 0 \end{cases} \tag{3.41}$$

with

$$\mu = r + g(m^2 + S) \tag{3.42}$$

and putting to zero the time derivatives, from Eqs. (3.37), (3.38) and (3.39) we obtain the set of equations

$$(\lambda + \mu)m = h \tag{3.43}$$

$$\omega(k) C_\perp(\vec{k}) = T \tag{3.44}$$

$$S = \frac{1}{V} \sum_{\vec{k}} C_\perp(\vec{k}). \tag{3.45}$$

In order to solve for m and $C_\perp(\vec{k})$, the strategy is to use the above equations to convert Eq. (3.42) into an equation for μ, to solve it and then to insert the solution back into Eqs. (3.43) and (3.44).

In the case $h \neq 0$ and $T \neq 0$, from Eq. (3.36) follows $C_\perp(\vec{k}) \geq 0$, hence Eq. (3.44) implies $\omega(k) \geq 0$, which, in turn, because of Eq. (3.41), requires

$$\mu \geq \mu_{min} = -k_{min}^2 \sim L^{-2} \tag{3.46}$$

where $k_{min} \sim 1/L$ is the minimum allowed value of $k \neq 0$. Therefore, for a given λ and for V sufficiently large, $\lambda + \mu > 0$ and Eq. (3.43) can be rewritten as

$$m = \frac{h}{\lambda + \mu}. \tag{3.47}$$

In the same way, from Eq. (3.44) we can write

$$C_\perp(\vec{k}) = \begin{cases} T/(\lambda + \mu), & \text{for} \quad k = 0 \\ T/(k^2 + \mu), & \text{for} \quad k \geq k_{min} \end{cases} \tag{3.48}$$

where $C_\perp(\vec{k}_{min})$ diverges as μ approaches μ_{min}. Inserting the above results into Eq. (3.42), one finds

$$\mu - g\left(\frac{h}{\lambda + \mu}\right)^2 = r + \frac{g}{V}\frac{T}{\lambda + \mu} + \frac{Tg}{V} \sum_{\vec{k} \neq 0} \frac{1}{k^2 + \mu}. \tag{3.49}$$

For V sufficiently large the second term in the right hand side can be neglected and, for the sake of clarity, the equation can be rewritten in the form

$$\mu - g\left(\frac{h}{\lambda+\mu}\right)^2 = r + \frac{g}{V}\frac{T}{\mu-\mu_{min}} + \frac{Tg}{V}\sum_{\vec{k}>\vec{k}_{min}}\frac{1}{k^2+\mu} \tag{3.50}$$

where the k_{min} term has been extracted from underneath the sum. Letting μ to vary over $[\mu_{min},\infty)$, the left hand side is a monotonously increasing function of μ, while the right hand side is a function divergent at μ_{min} and monotonously decreasing with increasing μ. Therefore, for any finite V, there exists a solution $\mu^*(V) > \mu_{min}$. Therefore, for any finite V, there exists a solution $\mu^*(V) > \mu_{min}$. Looking at Eqs. (3.47) and (3.48), this means that the system behaves paramagnetically all over the (T,h) plane, with a finite structure factor. The difference with respect to what one would have in the purely ferromagnetic model, due to $\lambda \neq 0$, is revealed by the anomaly (3.48) in the structure factor at $k = 0$ and by the reduction of the magnetization in Eq. (3.47). Rewriting the latter as $\mu^*(V)m = h_{eff}$ with

$$h_{eff} = h - \lambda m, \tag{3.51}$$

we see that the reduction of the magnetization comes about through a feedback mechanism, whereby the external field h, via the antiferromagnetic interaction, is substituted by h_{eff}.

Let us now see what happens in the infinite volume limit. Taking the infinite volume limit $\mu_{min} \to 0^-$ and there are two possibilities

$$\lim_{V\to\infty}\mu^*(V) = \begin{cases} \mu^* > 0 \\ \mu^* = 0. \end{cases} \tag{3.52}$$

In the first case, the second term in the right hand side can be neglected and Eq. (3.50) takes the form

$$\mu - g\left(\frac{h}{\lambda+\mu}\right)^2 = r + TgB(\mu) \tag{3.53}$$

where

$$B(\mu) = \lim_{V\to\infty}\frac{1}{V}\sum_{\vec{k}\neq 0}\frac{1}{k^2+\mu} = \int\frac{d\vec{k}}{(2\pi)^d}\,\frac{1}{k^2+\mu}. \tag{3.54}$$

Eq. (3.53) does, indeed, to have a positive solution if T is greater than the h-dependent critical temperature

$$T_C(h) = -\frac{r + gh^2/(\lambda)^2}{gB(0)} \tag{3.55}$$

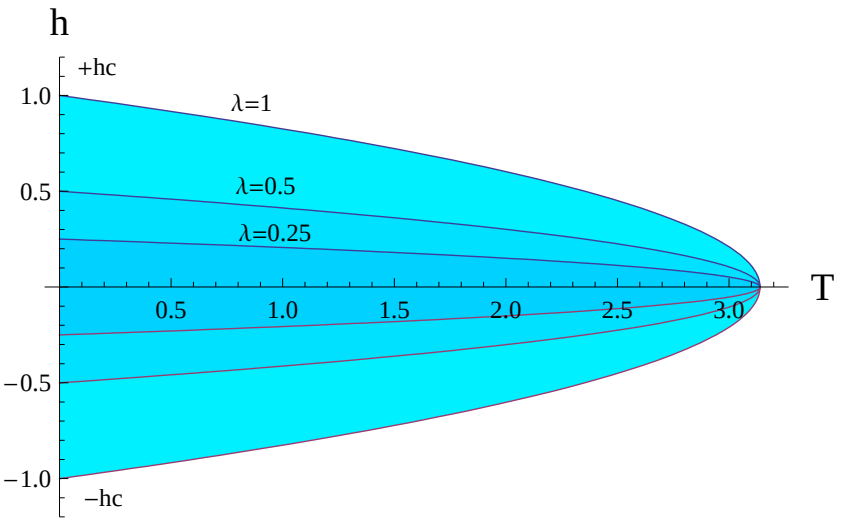

Figure 3.2: Phase diagram for the system. The region such us $T < T_c(h)$ and $h < h_c$ are the zone of phase coexistence and separation. The amplitude of the phase separation region depends on the value of λ, the coupling of the long-range anti-ferromagnetic interaction.

with

$$B(0) = K_d \int_0^\infty dk \, \frac{k^{d-1} e^{-k^2/\Lambda^2}}{k^2} \tag{3.56}$$

and where K_d is the d dimensional solid angle, while Λ is an high momentum cutoff. For $d \leq 2$, $B(0)$ is a divergent quantity, yielding $T_C(h) = 0$ for any h. Instead, if $d > 2$, $B(0)$ is finite and $T_C(h)$ reaches the maximum value $T_C(0) = -r/gB(0)$ for $h = 0$, decreasing to zero when h reaches the limit value Fig. 3.2.

$$h_C = \pm\lambda(-r/g)^{1/2}. \tag{3.57}$$

Conversely, if (T, h) are such that $T < T_C(h)$, Eq. (3.53) cannot be satisfied. This means that the second of the two possibilities in Eq. (3.52) applies, requiring to keep also the second term in the right hand side of Eq. (3.50), which we rewrite as

$$\mu - g\left(\frac{h}{\lambda+\mu}\right)^2 = r + \frac{g}{V} C_\perp(\vec{k}_{min}) + \frac{Tg}{V} \sum_{\vec{k}>\vec{k}_{min}} \frac{1}{k^2+\mu} \tag{3.58}$$

and, since this is satisfied for $\mu = 0$, we finally get

$$C_\perp(\vec{k}_{min}) = V\left[-\frac{r}{g} - \left(\frac{h}{\lambda}\right)^2\right]\left[\frac{T_C(h) - T}{T_C(h)}\right] \tag{3.59}$$

showing that $C_\perp(\vec{k}_{min})$, for $T < T_C(h)$, diverges like the volume in order to give a finite contribution.

Summarizing, for any finite V there exists a solution $\mu^*(V) > \mu_{min}$ of the self-consistency Eq. (3.50), which gives

$$m = \frac{h}{\lambda + \mu^*(V)} \tag{3.60}$$

and

$$C_\perp(\vec{k}) = \frac{T}{k^2 + \mu^*(V)}. \tag{3.61}$$

When the limit $V \to \infty$ is taken, these become

$$m = \begin{cases} h/(\lambda + \mu^*), & \text{for} \quad T > T_C(h) \\ h/\lambda, & \text{for} \quad T < T_C(h) \end{cases} \tag{3.62}$$

where $\mu^* > 0$, and

$$C_\perp(\vec{k}) = \frac{T}{k^2 + \mu^*} \tag{3.63}$$

for $T > T_C(h)$, while for $T < T_C(h)$ a condensate appears

$$C_\perp(\vec{k}) = \frac{T}{k^2} + \mathcal{M}^2(T)\delta(\vec{k} - 0^-) \tag{3.64}$$

where

$$\mathcal{M}^2(T) = \left[-\frac{r}{g} - \left(\frac{h}{\lambda}\right)^2 \right] \left[\frac{T_C(h) - T}{T_C(h)} \right] \tag{3.65}$$

is the condensate at k_{min}.

The presence of a peak in the correlation function is a manifestation of a coarsening process and it is sign of phase separation.

In order to understand this result, it should be recalled that in the purely ferromagnetic large N model the phase transition occurs only on the $h = 0$ axis, where for $T < T_C(0)$ the condensation of fluctuations at $k = 0$ takes place [31]. Condensation of fluctuations means that $C_\perp(\vec{k} = 0)$ becomes macroscopic in order to equilibrate the system below $T_C(0)$ without braking the symmetry, through a mechanism very similar to that of the Bose-Einstein condensation [51]. No other mechanism is available, since the large N limit renders the system effectively Gaussian [31, 32]. However, condensation of fluctuations, through the appearance of the Bragg peak at $\vec{k} = 0$, produces exactly the same phenomenology of the structure factor as that of phase separation in the nonlinear models [12]. Instead, when $h \neq 0$ the symmetry

is broken and equilibrium can be established at any temperature through the development of a non vanishing magnetization.

In the system with the antiferromagnetic coupling everything remains the same along the $h = 0$ axis, since the symmetry is unbroken, the magnetization is zero and the only effect of the λ term is to shift the condensation Bragg peak from $\vec{k} = 0$ to $\vec{k} = 0^+$. The novelty appears outside of the $h = 0$ axis, where there is a non vanishing magnetization and the feedback mechanism producing the effective reduction (3.51) of the external field is operating. So, if for a given λ, the values of (T, h) manage to make $h_{eff} = 0$, then condensation of fluctuations must take place in order to equilibrate the system even for $h \neq 0$. The result is the phase diagram of Fig. 3.2, showing the expansion of the phase coexistence region outside the $h = 0$ axis. The constant λ curves delimit the regions on the (T, h) plane within which the system self-tunes the final magnetization to the value such that $h_eff = 0$ and triggering, therefore, the condensation of the $\vec{k} = 0^+$ fluctuations.

3.4.2 Dynamical properties

Going back to the dynamical problem, the eqs. (3.37), (3.38) and (3.39). can be easily solved numerically.

We solve the coupled equations (3.37), (3.38) and (3.39) in a discretized tridimensional Fourier space. The equations are solved with fourth-order Runge Kutta method with adaptive step size [29]. We use a mesh of $L = 1000$ with $V = L^d$.

First let us consider (T, h) in the region of phase separation, namely for $T < T_c(h)$. The solution of equation for magnetization (3.37), starting from each initial conditions, reaches the equilibrium value

$$m_{eq} = \frac{h}{\lambda}. \tag{3.66}$$

which makes $h_{eff} = 0$ in Eq. (3.51), as explained above. The behavior of the magnetization shown in Fig. 3.3 agrees quite well with that obtained by Monte Carlo simulations in the discrete spin model of Ref. [23].

For $T < T_c(h)$, we obtain the magnetization behaviors shown in Fig. 3.3, in agreement with [23], obtained by Monte Carlo simulations. After a short time the magnetization reaches the equilibrium value.

The transverse structure function shows the appearance of a condensate a $k = k_{min}$ (Fig. 3.4). The condensate $C(k_{min})$ grows in the late stage of evolution as a power low $C(k_{min}) \sim t^{d/2}$. This is the signature of the universality class of non-conserved order parameter ordering systems. The appearance of a condensate is the confirmation of a phase separation in the

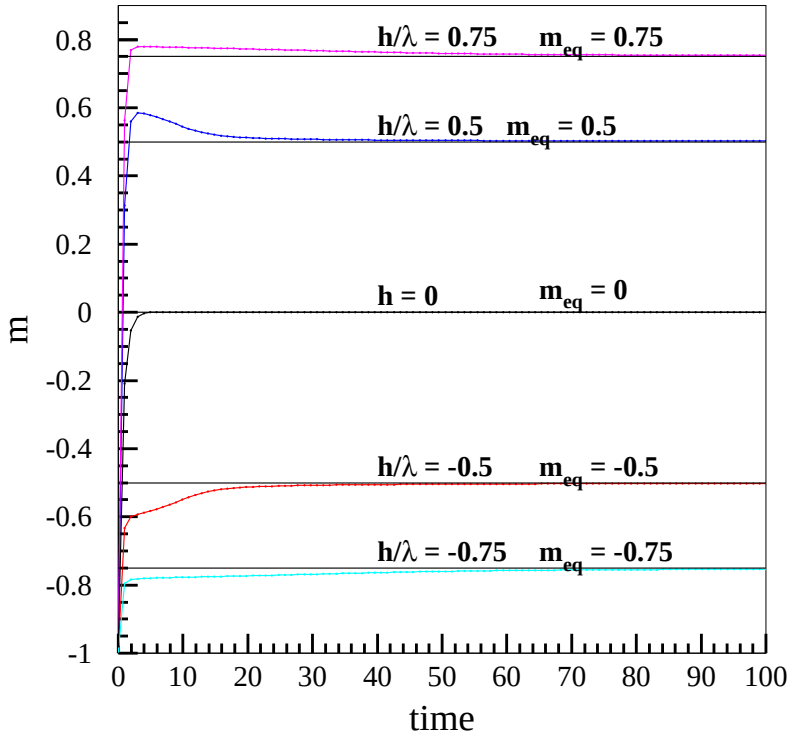

Figure 3.3: Evolution in the time for the magnetization. We chose $g = -r = 1$, and $T < T_c(h)$. and $m(t = 0) = -1$. The asymptote is $\frac{h}{\lambda}$.

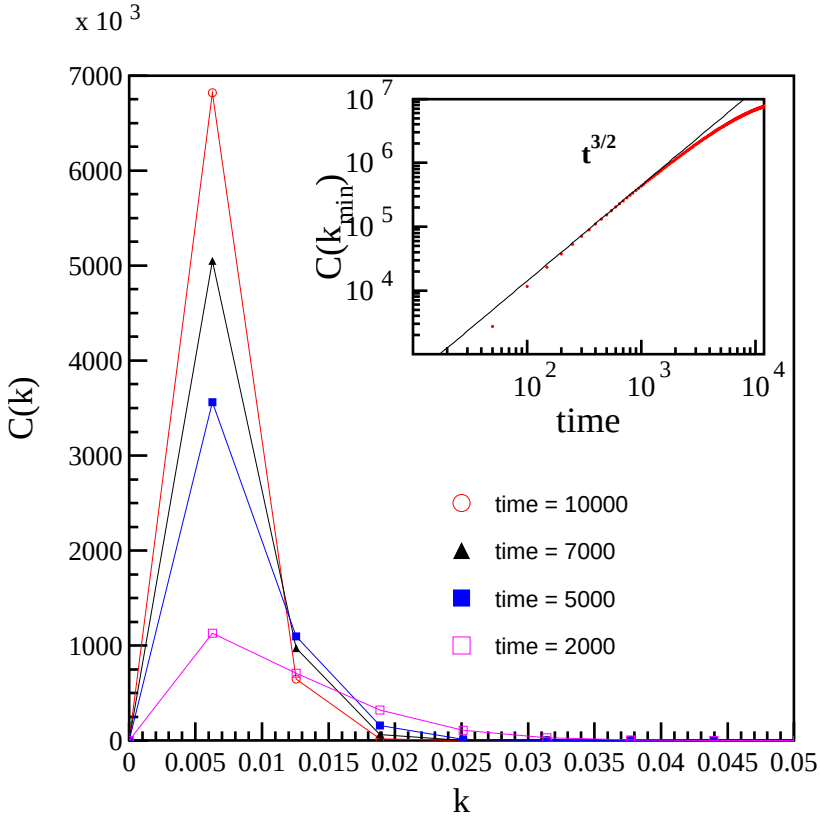

Figure 3.4: Evolution of correlation function $C(k)$ for $T < T_c(h)$. Inset: evolution of the condensate $C(k_{min})$

N infinite scheme. Let us note that the evolution of magnetization density $m(t)$ is much faster than the phase ordering characterized by a coarsening of the correlation regions. So we can distinguish a fast process which is the tuning of the stable value of the magnetization and a lower process which is the phase separation.

If $T > T_c(h)$ there is a solution of the auto-consistence relation without condensate. This implies that equilibrium value of magnetization is $m_{eq} = \frac{h}{\lambda+\mu^*}$ as is showed in Fig. 3.5 and the peak of transverse correlation function is of order of unityes (inset of Fig. 3.5). The region $T > T_c(h)$ has no phase separation.

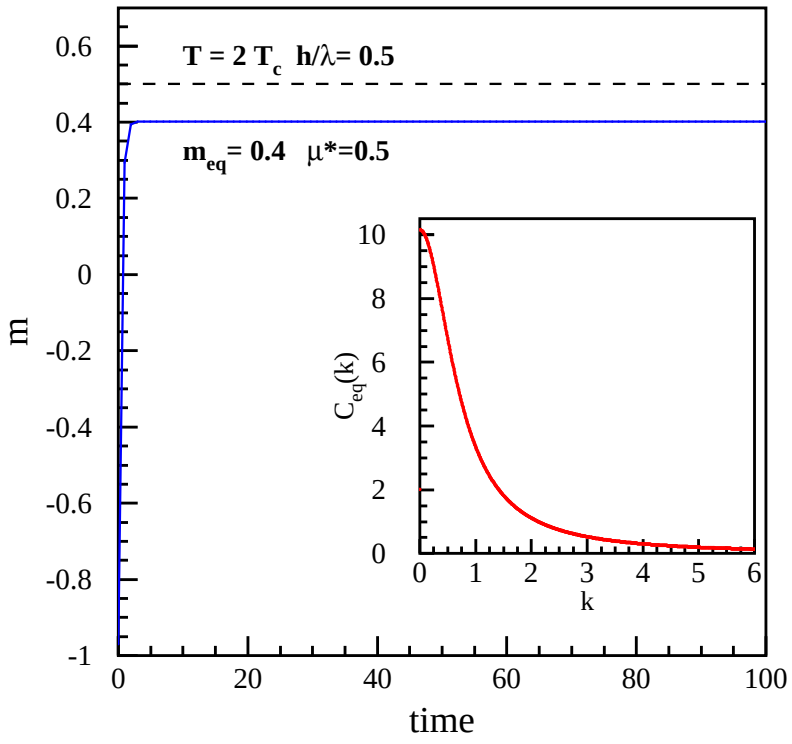

Figure 3.5: Behavior of magnetization for (T,h) such as $T > T_c(h)$. The dotted line represents the equilibrium value of magnetization if $T < T_c(h)$. Inset: behavior of the equilibrium transverse structure factor $C_{eq}(k)$, for each k $C_{eq}(k) = \frac{T}{k^2+\mu^*}$.

3.5 Discussion

The model presented in the chapter 2 and published in [23] inspirated the treatment of an Hamiltonian composed by a short-range ferromagnetic interaction, a long-range antiferromagnetic interaction and an interaction with an external magnetic field. The system has the peculiarity to show phase coexistence for sub-critical temperature in presence of an external magnetic field. We investigated this behavior deriving the Langevin motion equations in the $N \to \infty$ limit. Thanks to the large N scheme we obtained the analytical form of the critical temperature as function of magnetic field and antiferromagnetic coupling λ. The phase diagram in (T, h) plane shows the phase coexistence regions for a given λ for all the values of h such that $h < h_C = \pm\lambda(-r/g)^{1/2}$. The equilibrium value of magnetization $m_{eq} = h/\lambda$ is in agreement with to one obtained in the Monte Carlo simulation for a lattice gas system. The systems shows, for $T < T_C$, an increasing Bragg peak in the transverse correlation function. The peak is the demonstration of phase separation and represents, in the case of scalar field, the formation of domains. The late time behavior of the correlation function is characterized by a scale invariance which is marked by a power low behavior of the Bragg peak as function of the time. For a tridimensional system the growing exponent of power low is $\frac{3}{2}$. It is possible to demonstrate [30] that $3 = d$ with d the euclidean dimension, therefore the growing exponent is $\frac{1}{2}$ according to the scheme of non conserved order parameter and to the behavior of mean cluster size in [23]. The general property of the functional in creating a region of phase coexistence can be very useful in other systems where a balance between a magnetic field and long-range repulsion self-tunes the system in a state of phase coexistence in the presence of an external field.

Chapter 4

Large N model for anisotropic magnetic field

In the presence of a gradient in the magnetic field the spatial symmetry of the system is explicitly broken. In this chapter we derive the Langevin equations of motion and we present some numerical results regarding the behavior of magnetization and equal time correlation function when the external field is anisotropic. Then we discuss the obtained results.

4.1 Langevin equation of motion

Let us now consider the case of the Hamiltonian (3.15) with an anisotropic magnetic field. To respect boundary periodic conditions we use this magnetic field

$$h(x) = h_0 + \epsilon h_0 cos(2\pi x/L), \tag{4.1}$$

where h_0 is the average amplitude and ϵ is a little percentage of anisotropy. We consider the Langevin equation of motion of form (3.17). Fourier transforming with respect to space and introducing the equal-time transverse structure function, at leading order we have the following close set of equations (see appendix A and B for the details of calculations):

$$\begin{aligned} \frac{\partial m(\vec{k},t)}{\partial t} &= -(k^2+r)m(\vec{k},t) - \lambda m(0,t)\delta_{\vec{k},0} + \\ &\quad -\frac{g}{V^2 N}\sum_{\vec{p},\vec{q}} m(\vec{k}-\vec{p}-\vec{q},t)m(\vec{p},t)m(\vec{q},t) + \\ &\quad -\frac{g}{V}\sum_{\vec{q}} S(\vec{k}-\vec{q},t)m(\vec{q},t) + h(\vec{k}), \end{aligned} \tag{4.2}$$

$$\begin{aligned}\frac{\partial C(\vec{k}_1,\vec{k}_2,t)}{\partial t} &= -(k_1^2+k_2^2+2r)C(\vec{k}_1,\vec{k}_2,t) - \lambda[C(0,k_2,t)\delta_{\vec{k}_1,0} + C(0,k_1,t)\delta_{\vec{k}_2,0}] + \\ &-\frac{g}{V^2N}\sum_{\vec{p},\vec{q}}\{m(\vec{k}_1-\vec{p}-\vec{q},t)m(\vec{p},t)C(\vec{q},\vec{k}_2,t) \\ &+m(\vec{k}_2-\vec{p}-\vec{q},t)m(\vec{p},t)C(\vec{q},\vec{k}_1,t)\} + \\ &-\frac{g}{V}\sum_{\vec{q}} S(\vec{k}_1-\vec{q},t)C(\vec{q},\vec{k}_2,t) + S(\vec{k}_2-\vec{q},t)C(\vec{q},\vec{k}_1,t) \\ &+2T\delta_{\vec{k}_1+\vec{k}_2} \end{aligned} \tag{4.3}$$

and auto-consistence relation:

$$S(\vec{k}-\vec{q},t) = \frac{1}{V}\sum_{\vec{p}} C(\vec{k}-\vec{p}-\vec{q},\vec{p},t), \tag{4.4}$$

where $m(\vec{k},t)$ is the total magnetization, $C(\vec{k}_1,\vec{k}_2,t)$ is the equal time correlation function and $h(\vec{k})$ is the Fourier transform of $h(\vec{x})$. The $N\to\infty$ limit produces the auto-consistence relation 4.3.

The derived equations are quite complicated. For simplicity we derive numerical solution in the case of one-dimensional system. In the large N limit the critical temperature at $d=1$ is $T_C=0$, so we solve the set of equations (4.3), (4.4) and (4.1) at $d=1$ and $T=0$.

4.1.1 Numerical solution at $d=1$ and $T=0$

In the Fourier one dimensional space the expression for the magnetic field is:

$$h(k) = h_0\delta_{k,0} + h_0\frac{\epsilon}{2}(\delta_{k,k_{min}} + \delta_{k,-k_{min}}). \tag{4.5}$$

Solving the equations (4.3), (4.4) and (4.1) with Runge Kutta method with adaptive step size [29], we obtain for the equilibrium magnetization an anisotropic spatial behavior (Fig.4.1). The magnetization anisotropy is as so deep as ϵ is larger. The component $k=0$ is the value the total magnetization, and after a transient, we have $m/V = 1/L\int_L m(x)dx \sim \frac{h_0}{\lambda}$ in agreement with the Monte Carlo results and with the large N isotropic case.

For the equal time correlation function $C_{eq}(k_1,k_2)$ we obtain the behavior shown in Fig.4.2. The function presents two peaks corresponding to the coordinates $(k_1,k_2)=(-k_{min},k_{min})$ and $(k_1,k_2)=(k_{min},-k_{min})$, this is clearly an effect of the shape of $h(k)$.

Let us to observe that in the case of $T=0$ the final behavior is dependent on the initial condition for for $C(k_1,k_2,t=0)$.

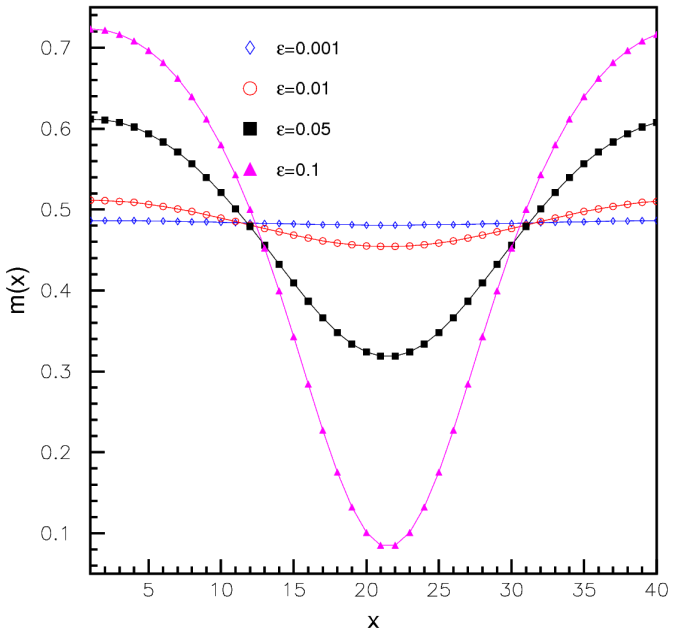

Figure 4.1: Behavior of equilibrium magnetization for $T = 0$ for different values of anisotropy percentage of magnetic field.

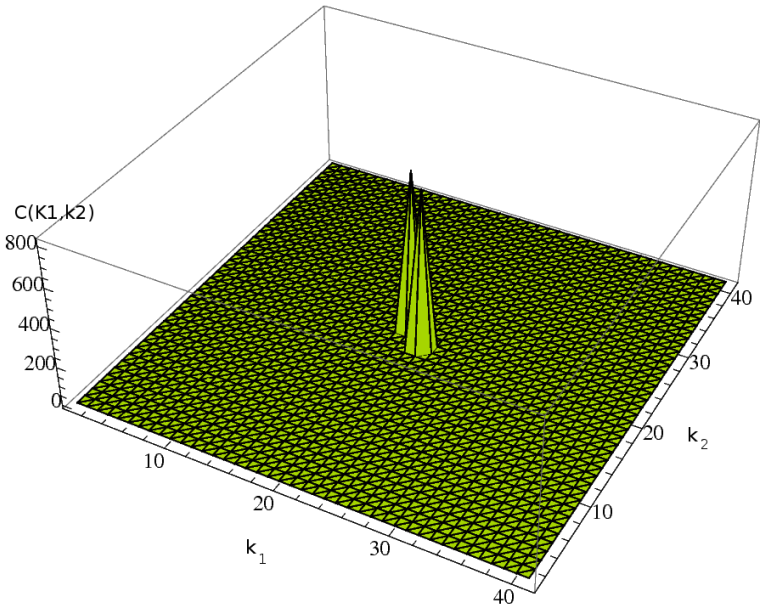

Figure 4.2: Behavior of equilibrium $C_{eq}(k_1, k_2)$ at $T = 0$.

- $C(k_1, k_2, t = 0) > 0$ and for any $m(k, t = 0)$. With these initial conditions the system evolves in the configuration for magnetization showed in Fig.4.1.

- $C(k_1, k_2, t = 0) = 0$ and for any $m(k, t = 0)$. In this case the equilibrium magnetization behavior is not proportional to the anisotropy. The magnetization profile amplify the anisotropy and the process is faster if the anisotropy is larger (Fig. 4.3). The correlation function doesn't evolve and it is always null.

The second solution is unstable because for any $C(k_1, k_2, t = 0) > 0$ the system will evolve to reaches the first solution. However in the case of $T > 0$ for dimension of space $d \geq 3$ we expect a magnetization behavior similar to the observed in (Fig.4.2). In this case, in fact, $C_{eq}(k_1, k_2)$ will be greater than zero also if $C(k_1, k_2, t = 0) = 0$, being $T > 0$.

4.1.2 Observations and discussion

Ferromagnetic anisotropic case To have a complete pictures of the obtained results it is convenient to consider first the case of magnetization of a simple ferromagnetic interaction, corresponding to $\lambda = 0$. The external field acting

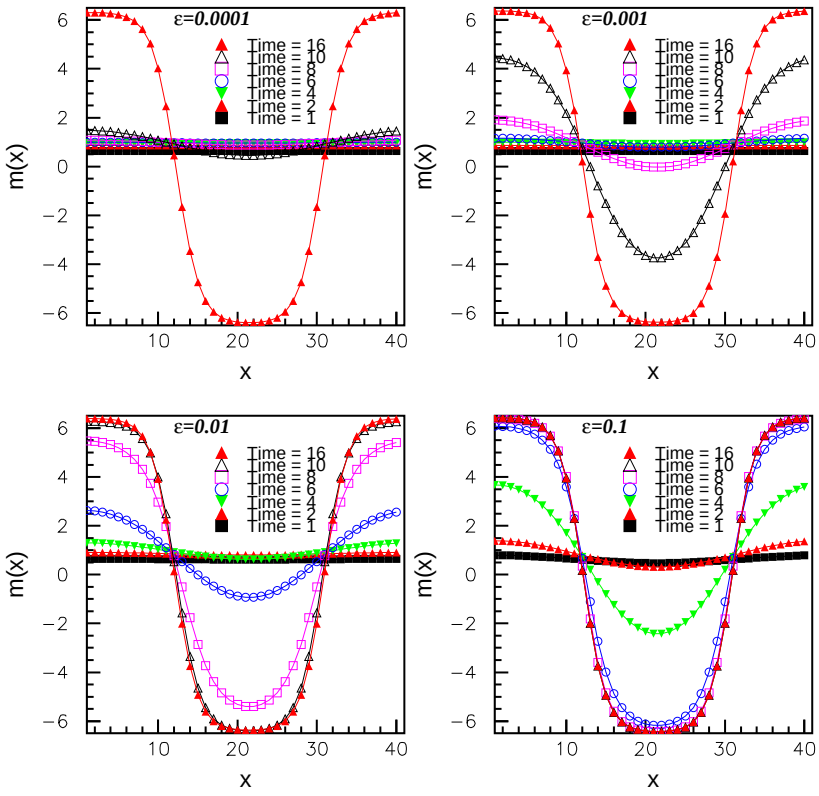

Figure 4.3: Profile of $m(x)$ at different times for 4 values of anisotropy ϵ. The phase separation process is faster for the higher values ofϵ but the final state is the some.

on a pure ferromagnetic system is not uniform. Then also the equilibrium magnetization want be not uniform and must satisfy the equation

$$\left[-\frac{d^2}{dx^2}+r+gm^2(\vec{x})+gS(\vec{x})\right]m(\vec{x})=h(\vec{x}) \tag{4.6}$$

obtained by (3.28). let us consider the case of a field in the form

$$h(\vec{x})=\epsilon f(\vec{x}) \tag{4.7}$$

where ϵ is a small parameter and $f(\vec{x})$ is a smoothly function taking positive and negative values in such a way that $\overline{f}=0$. We are interested in the behavior of $m(\vec{x})$ in the infinite volume limit. Neglecting the nabla squared contribution, from Eq. (4.6) follows

$$m=\begin{cases} b(T)h(\vec{x}), & \text{for} \quad T>T_C(h) \\ m(T)(h(\vec{x})/|h(\vec{x})|)+c(T)h(\vec{x}), & \text{for} \quad T<T_C(h) \end{cases} \tag{4.8}$$

where $m(T)$ is the spontaneous magnetization of ferromagnetic system, while $b(T)$ and $c(T)$ are temperature dependent coefficients of order ϵ. Namely, for $T<T_C$, locally there is spontaneous magnetization with the sign of the external field. The above result is expected to be correct if the free energy cost of space inhomogeneities in the magnetization, due to the nabla square contribution, is smaller than the gain for having a magnetization following the external field. A simple argument of the type used for the critical radius of the nucleation droplets, yields

$$R\geq 1/\epsilon \tag{4.9}$$

where R is the typical distance for the variations of $h(\vec{x})$.

If the magnetic field is of the form

$$h(\vec{x})=h_0+\epsilon f(\vec{x}) \tag{4.10}$$

a little anisotropy $\epsilon>0$ is not sufficient to amplify the anisotropy of magnetization which shows only a very ligth anisotropy. The magnetization is almost uniformly positive if $h_0>0$ and almost uniformly negative if $h_0<0$.
Antiferromagnetic anisotropic case Adding the antiferromagnetic coupling λ, for $d=1$ we can write

$$\left[-\frac{d^2}{dx^2}+r+gm^2(x)+gS(x)\right]m(x)=h_0-\lambda\overline{m}+\epsilon f(x) \tag{4.11}$$

Let us, then, assume that the non uniform magnetization can be written as

$$m(x)=m_0+\delta m(x) \tag{4.12}$$

where $\delta m(x) \sim O(\epsilon)$ and m_0 is the solution of the uniform equation

$$r + gm^2 + gS_0 m_0 = h_0 - \lambda m_0. \tag{4.13}$$

A similar expansion is assumed to hold for S(x)

$$S(x) = S_0 + \delta S(x) \tag{4.14}$$

also with $\delta S(x) \sim O(\epsilon)$. Keeping only the first order terms, Eq. (4.11) becomes

$$\left[-\nabla^2 + r + 3gm^2 + gS_0\right] \delta m(x) = \epsilon f(x) - gm_0 \delta S(x). \tag{4.15}$$

Fourier transforming, considering that $r + gm_0^2 + gS_0 = 0$ in autoconsistency way and $m_0 = h_0/\lambda$, we have

$$\delta m(x) = \frac{\epsilon f(k) - gm_0 \delta S(k)}{k^2 + 2gm_0^2} \tag{4.16}$$

which shows that, indeed, $\delta m(x) \propto \epsilon$ since $k^2 + 2gm^2 > 0$, in agreement with the numerical results shown in Fig. 4.1. The above considerations do apply for $T > 0$ and also for $T = 0$, if $C(k) \neq 0$ in the initial condition, at least for some k. Instead, if $T = 0$ and $C(k) = 0$ in the initial condition, then $S(x,t) = 0$ for all time, i.e. the transverse components do not play any role and the magnetization evolves like in the scalar model governed by the time dependent Ginzburg-Landau equation

$$\frac{\partial m(x)}{\partial t} = -\left[-\frac{d^2}{dx^2} + r + gm^2\right] + (h - \lambda \overline{m}). \tag{4.17}$$

The equilibrium magnetization, in the uniform case, is the solution of $(r + \lambda)m_0 + gm_0^3 = h_0$. Let us than see if the solution in the non uniform case is analytic in ϵ, as in the previous case. Using (4.13), Eq. (4.17) at equilibrium yields

$$\left[-\frac{d^2}{dx^2} + r + 3gm_0^2\right] \delta m(x) = \epsilon f(x). \tag{4.18}$$

Fourier transforming this gives

$$[k^2 + r + 3gm_0^2]\delta m(k) = \epsilon f(k) \tag{4.19}$$

which yields $\delta m(k) \sim O(\epsilon)$ only if $(k^2 + r + 3gm_0^2) > 0$. However, if the values of h_0 and λ give a solution such that $(r + 3gm_0^2) < 0$, than there can be a value of k such that $[k^2 + r + 3gm_0^2] = 0$. In that case, even if the corresponding

$f(k) = 0$, it is not guaranteed that there is analiticity in ϵ. This is what seems to happen from the numerical solution, since $\delta m(x)$ is not proportional to ϵ for small ϵ. This argument can explain the behavior observed in Fig. 4.3, where there is no continuity of the magnetization anisotropy respect to the external anisotropy.

Large N model and domains The spatial behavior of magnetization for the stable solution Fig. 4.1 is not in exact agreement with the Monte Carlo simulations, where the spatial phase separation is very sharp also for very small gradient of field Fig. 2.5. The discrepancy steads in the different nature of the two models. The discrete model presented in chapter 2 is a scalar model and there is a straight correspondence between total magnetization m and magnetization inside the domains m_D, in fact $m = (m_D V_+ - m_D V_-)/V$ with $V_\pm$ the volume of the positive and negative phase respectively. In the large N model, instead, the total magnetization lies in the parallel direction, but the fluctuations, which characterize the coarsening process are in the normal direction, so they are decoupled from magnetization. In the large N description it is not proper to speak of domains and the phase separation process doesn't characterizes the magnetization spatial behavior but produces, in the transverse structure function, the appearance of a condensate. The large N results are to be intended exactly corresponding to the scalar cases for the total magnetization an for the scaling behavior of the condensate in the time.

Chapter 5

Study of fractal behavior in Vasculogenesis

Chemotaxis has an important role in the morphogenesis of organs and tissues, this role is clearly evident in the developing of vascular networks. Here we show a study of chemoattractant effective radius on fractal behavior of bi-dimensional simulated vascular networks.

The chapter is organized as follow: a brief introduction on the characteristic of vasculogenesis process, the description of the lattice-gas model used for simulation, the general formalism adopted to characterize the simulated structures and finally the Monte Carlo results and the discussion.

5.1 Introduction

To supply tissues with nutrients in an optimal way, vertebrates have developed the hierarchical vascular system which starts from big vessels and terminates in a network of capillaries.

Vascular networks are made of endothelial cells. Their growth is essentially driven by two processes: vasculogenesis and angiogenesis [45]. Vasculogenesis is the de novo growth of the primary vascular network from initially endothelial cells and it is the first step in the development of the circulatory system in vertebrates. In the first stages of vasculogenesis, endothelial cells autorganizes in a network-like structure, called the primary capillary plexus, which subsequently remodels, with the size of the vacancies between ribbons of endothelial cells coarsening over time. Angiogenesis is, essentially, characterized by sprouting of an immature structure and remodeling.

Experiments made with HUVEC (human umbilical vein endothelial cells) randomly spread on gel matrix, which favors cell motility and has biochem-

ical characteristics similar to living tissues, self-assemble to form geometric tubular networks Fig. 5.1, which are almost identical to capillary vascular beds observed in living beings [42].

Several studies have been performed to understand the logic of vascular network growth. For example Manoussaki and coworkers [43] proposed a theoretical model based on cellular traction, recently Szabo and coworkers [44] focus on the attraction between elongated structures and they show a theoretical model based on this observation.

One of the mechanism most appreciated by biologist has chemotaxis as fundamental mechanism for cell to cell communication. An accurate statistics of individual cells trajectories presented in [42], shows that in the first phase cell motion has marked persistence in the initial direction, pointing toward zones of higher concentrations of cells. This indicates that cells communicate among them through the emission of soluble chemical factors that diffuse and degrade in the surrounding medium, and suggests that they move toward the gradients of this chemical field. Cells produces specifics attractants which diffuse and, after some time, degrades. The distribution of chemoattractant becomes anisotropic leading the endothelial chemotacting cells to follows the local gradients. First of all this idea was developed by Gamba et al. [40] in a continuous model and subsequently used in a discrete cell centered model based on lattice-gas by Merks et al [39].

The study of vascular networks is very useful, in fact the growth of blood vessels in the developing organs is basically the result of an invasion process by capillaries into the early organs's structures. It has been proven and accepted that during tumorogenesis angiogenesis is essential to provide the requisite nutritional supply to growing tumors [45].

From a physical point of view, there are two important features in vasculogenesis observed in vitro experiments: autosimilarity of formed structures and the percolative behavior of process. The vascular network is an example of natural structure characterized by emerging of self-similarity and non trivial scaling laws. The formed patterns often show self-similarity and scaling laws similar to those emerging in the physics of phase transitions and of several kinds of aggregation dynamics. For many of these systems it has been shown that scaling laws are directly related to the process which led to the formations of the structure itself.

Self-similar object shows often fractal behavior [46, 48, 42]. Fractal analysis is widely used in the study of vascularization because it is a convenient method that defines the complexity and it can discriminate the growing process of natural structures. For example normal and tumoral vascular networks have different fractal dimensions. Different kind of growing factors (chemoattractants) or contact conditions for endothelial cells in the vessel

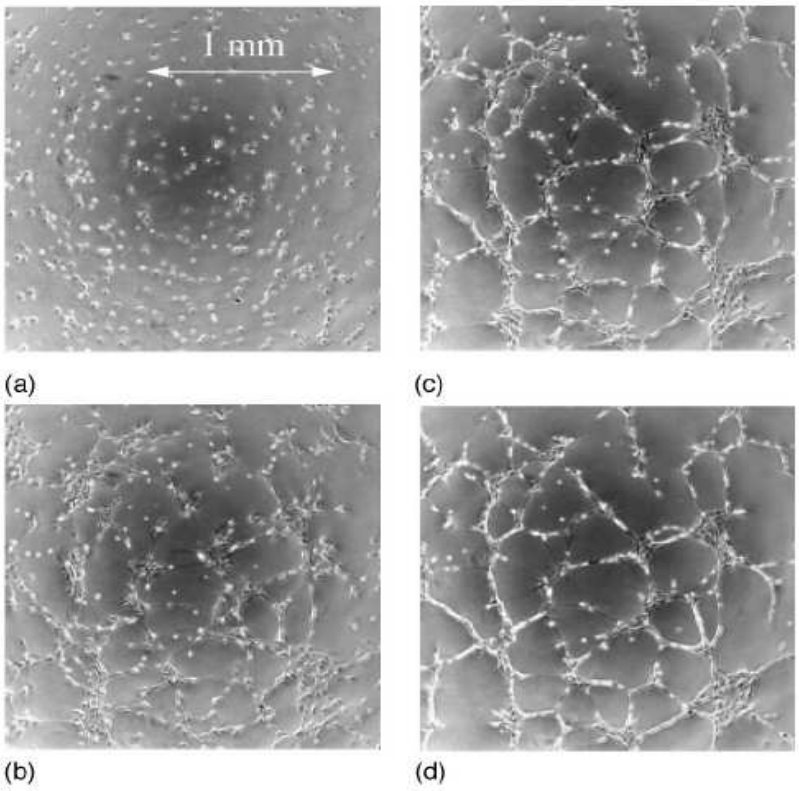

Figure 5.1: Experimental pictures of the dynamical process of vascular network formation obtained starting with an initial cell density of 200 cells/mm^2. (a) t = 0h ; (b) t = 3h ; (c) t = 6h ; (d) t = 9h . The side of the box is 2 mm. Observe that bright spots and darker edges appearing in the pictures are an artifact of phase-contrast microscopy but all correspond to the same kind of cellular matter. On the other hand, the Matrigel background is easily recognizable from the homogeneous gray color.

developing can give rise to different kind of fractal behaviors.

Another important characteristic of vascular networks in vitro is the percolating behavior [40]. There is specific cell density which permits the formation of a macroscopic connected network which crosses the entire system (percolating cluster), below this density there are small disconnected parts of network, whereas for very high density the cells organize in a very compact structure (swiss cheese configuration) Fig 5.2.

In nature there are different isoforms of growing factors for vasculogenesis. Experimental observations suggest that different possible kind of chemoattractant can give rise to different fractal structures [46, 47]. In this thesis we focus on the role of chemoattractant on vascular networks, in particular we investigate the effect of an effective interaction length generated by the chemotactic factor. The description in term of a chemoattractant regulated mechanism offer a natural interaction length given which is an effective attractant radius. It was showed in the model [40] in good agreement with experiments that this radius has a role in the fractal structures of vascular networks.

In this chapter we show a study of fractal dimension of simulated vascular networks for different values of the effective radius of autocrine chemoattractant. We model the vascular networks by Cellular Potts Model [39].

5.2 The Cellular Potts model

The model used for simulate the system is the Glazier and Grainer's Cellular Potts Model [37, 38, 39]. This is a lattice-gas model which represents endothelial cells on a rectangular, numerical grid, where the sites of identical non zero values represents a cell and a value of zero identifies the Extracellular Cellular Matrix (ECM).

The model is derived by the large q-Potts model describing a collection of N cells identifies by N spins $\sigma(x) = 1, 2, ...N$, where x identifies a lattice site. A cell consists of all sites in lattice with spin σ. There is a special spin value $\sigma(x) = 0$ which represents the ECM. The binding energy between cells and cells and ECM is regulated by the coupling J, and for mismatched bonds between different cells have energy $J_{\sigma(x),\sigma(x')}$ and bonds between like spins have energy 0. So the Hamiltonian is

$$\mathcal{H}_{potts} = \sum_{x,x'} J_{\sigma(x),\sigma(x')}(1 - \delta_{\sigma(x),\sigma(x')}). \tag{5.1}$$

We choose x' representing the six second order neighbors of x. An energy penalty increasing with cell's deviation from designated initial area A_σ con-

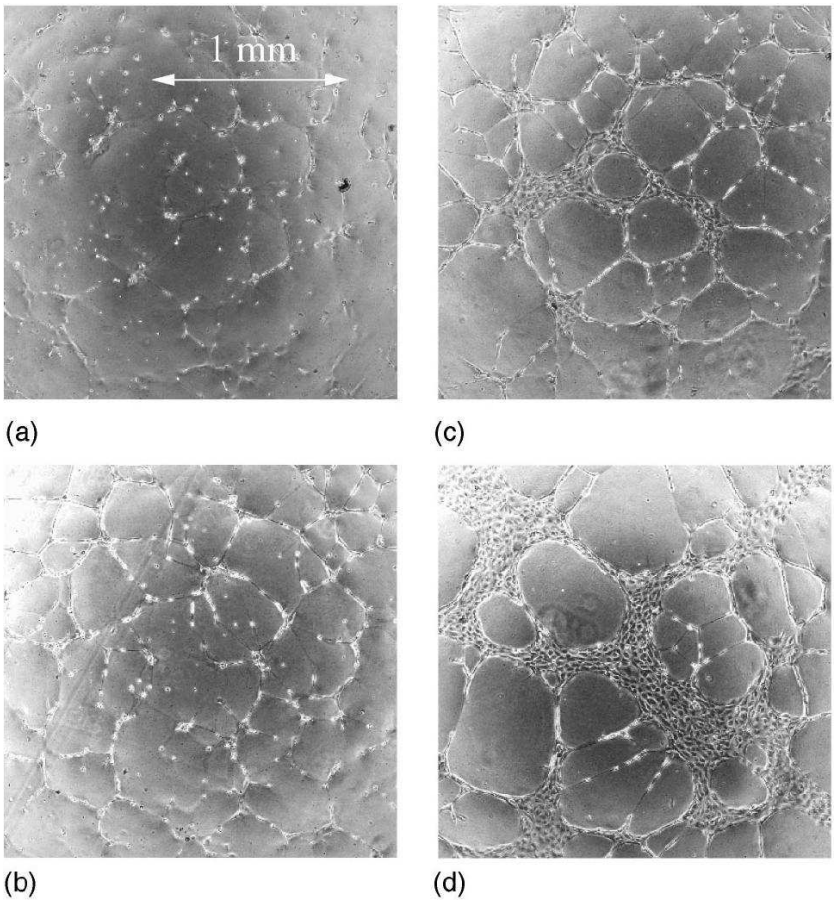

Figure 5.2: Experimental pictures of vascular structures obtained starting from four different values of the initial cell density. (a) 50 cells/ mm^2; (b) 100 cells/ mm^2; (c) 200 cells/ mm^2; (d) 400 cells/ mm^2. The side of the box is 2 mm. The critical density is about 200 cells/ mm^2.

straints the area of cells. The Hamiltonian becomes

$$\mathcal{H}_{potts} = \sum_{x,x'} J_{\sigma(x),\sigma(x')}(1 - \delta_{\sigma(x),\sigma(x')}) + \lambda \sum_{\sigma} (A_\sigma - a_\sigma)^2, \tag{5.2}$$

where λ is a Lagrange multiplier specifying the strength of the area constraint and a_σ is the temporary area of cell. To model the cell elongation regulated by cytoskeletal fluctuation a random site x of lattice is chosen and it is evaluated the probability to copy its spin $\sigma(x)$ into a randomly chosen neighbor x'. A Monte Carlo Step (MCS) is defined the time to perform $L \times L$ copies of randomly chosen sites. To model the attitude of cells to follow chemoattractant gradients there is an energy decreasing at time of copy

$$\Delta\mathcal{H}_{chemotaxis} = \gamma \left(c(x) - c(x') \right), \tag{5.3}$$

where $c(x)$ is the local concentration of chemoattractant. The total effective Hamiltonian is

$$\mathcal{H}_{vascolo} = \mathcal{H}_{potts} + \mathcal{H}_{chemotaxis}. \tag{5.4}$$

The description of the chemoattractant diffusion is performed by a macroscopic approximation using a concentration, in the some spirit of the model made by Gamba at [40, 41]. It is assumed that endothelial cells secrete with a rate α the chemoattractant $c(x,t)$, which degrades with rate ϵ and diffuse with a diffusivity D, obeing to the equation:

$$\frac{\partial c(x,t)}{\partial t} = \alpha(1 - \delta_{\sigma(x),0}) - \epsilon \delta_{\sigma(x),0} c(x,t) + D\nabla^2 c(x,t), \tag{5.5}$$

where $\delta_{\sigma(x),0} = 1$ out of the cell (on the ECM) and it is zero otherwise. From Eq. (5.5) $c(x,t)$ is produced on the cells and decays on ECM in a half life time $\tau = \epsilon^{-1}$ creating local gradients. The chemoattractant evolution provides a natural length scale $r_0 = \sqrt{D\tau} = \sqrt{\frac{D}{\epsilon}}$, which is the effective range of the interaction mediate by the soluble factor.

Summarizing, the model contains an effective energy and a diffusion equation. The movement of the cellular sites mimes the movement of the cell which extends the filiopoda in the direction of higher stimulation. The interaction of the cell with the substrate, the other cells and the chemoattractant are modeled by coupling constants in an effective energy function. The chemoattractant evolves by Eq. (5.5) and it contributes to the Hamiltonian by $\mathcal{H}_{chemotaxis}$.

We chose the following values for coupling constants: $J_{cell,cell} = 50$, $J_{cell,ECM} = 20$, $\lambda = 50$ and $\gamma = 1000$; and for diffusion equation: $\alpha =$

$2,8 \times 10^{-4} s^{-1}$, $D = 10^{-3} m^2 s^{-1}$, for ϵ we choose three values producing three values r_0. We perform a Monte Carlo simulation using the effective Hamiltonian then we solve numerically for 15 step the diffusion equation 5.5. The final time is $time = MCS \times \Delta t \times 15$ with Δt the temporal step for solving the equation. We chose $\Delta t = 2\ s$, whereas we chose the $\Delta x = 3\mu m$. We set the initial area of a cell to 13 sites, corresponding to a radius of cell of $\sim 8\mu m$. The parameters are chosen similar to [39].

5.3 General formalism

In this section we briefly illustrate the theoretical framework to treat the vascular networks as self-similar structures produced by percolative transition.

5.3.1 Fractal geometry

Fractal objects are scale invariant systems, whose volume scales with the linear size L following a power law with an exponent D lower that the Euclidean d dimension of the space in which it lives. The volume $V(L)$ may be measured by covering the fractal with d-dimensional boxes or spheres of linear dimension l with $l \ll L$, therefore $V(L) = N(L, l)$, where $N(L, l)$ is the number of such spheres. The exponent D is defined through the scaling of $N(L, l)$ as a function of decreasing L: for mathematical fractals $N(L, l)$ diverges as $L \to \infty$ following a power law behavior characterized by a non integer exponent:

$$N(L, l) \propto L^D \tag{5.6}$$

where

$$D = \lim_{L \to \infty} \frac{\ln N(L, l)}{\ln L}. \tag{5.7}$$

For fractals having a finite size and infinitely small ramifications, when the size of the covering balls $l \to 0$, $N(L, l) \propto l^{-D}$ with

$$D = \lim_{l \to 0} \frac{\ln N(L, l)}{\ln(1/l)}. \tag{5.8}$$

We note that the above definitions for non-fractals objects give a value of D which coincide with the Euclidean dimensions d of the embedding space.

5.3.2 Percolation

The purely geometric problem of percolation represents one of the simplest phase transition occurring in nature. It's s very useful for studying phase transitions (see appendix D) and for modeling several complex systems.

The percolation theory had been introduced at the end of 40th years by Flory and Stockamayer to study polymer physics [33, 34].

Many percolative models show a second-order phase transition in correspondence to a critical value of the density p p_c, i.e., the probability of observing an infinite cluster is 0 for $p < p_c$ and 1 for $p > p_c$ [35].

It is natural to chose as order parameter the probability P that a randomly chosen site belongs to an infinite cluster. If we define $N_s(p)$ the average number of clusters of mass s we can be write the order parameter as follow

$$P = p - \sum_s N_s s \tag{5.9}$$

while the analog of magnetic susceptivity in a ferromagnetic transition is the average cluster size

$$S = \frac{\sum_s N_s s^2}{\sum_s N_s s}, \tag{5.10}$$

where N_s is the number of clusters of size s, excluding from the sum the infinite cluster. S is the average size (number of sites) to which a randomly chosen occupied site in the lattice belongs.

The correlation (or connectivity) function $c(r)$ is defined as the probability that two randomly chosen sites at distance r are occupied on the same cluster and the correlation (or connectivity) length as

$$\xi^2 = \frac{\sum_s c(r) r^2}{\sum_s c(r)}, \tag{5.11}$$

where the sum is performed over sites.

In proximity of the critical point such quantities have the following behavior:

$$P = \begin{cases} 0 \quad if \quad p > p_c \\ \\ (p - p_c)^\beta \quad if \quad p > p_c \end{cases} \tag{5.12}$$

$$S \propto |p - p_c|^{-\gamma}, \tag{5.13}$$

The correlation length represents the mean cluster size of the finite clusters, and at critical point ($p = p_c$), ξ has a singularity in analogy to the thermodynamics systems:

$$\xi \propto |p - p_c|^{-\nu}, \tag{5.14}$$

The values of the critical exponent for Random Percolation are known exactly at d=2 and numerically at d=3, they are:

- $\nu = 4/3$ for $d = 2$, $\nu = 0.88$ for $d = 3$
- $\gamma = 43/18$ for $d = 2$, $\gamma = 1.80$ for $d = 3$
- $\beta = 5/36$ for $d = 2$, $\beta = 0.41$ for $d = 3$

For random percolation the behavior of percolating cluster is fractal and the fractal dimension is $D = 1.89$ for $d = 2$ and $D = 2.53$ for $d = 3$.

5.3.3 Finite -size scaling relations in percolation

Near the critical point a system is scaling invariant and as consequence it obeys to scaling relations.

The relation of the previous paragraph are valid for infinite systems, for finite systems, the relations are dependent on the system size. For scales less than ξ the system will be scaling invariant but for scales greater than ξ the system will have the behavior of a collection of independent system of linear length ξ. It possible to demonstrate [35] that for finite size L, the following relations are valid:

$$\Pi(p, L) \propto \Pi[(p - p_c)^{-1/\nu}], \tag{5.15}$$

$$P(p, L) \propto L^{-\beta/\nu} P[(p - p_c)L^{-1/\nu}], \tag{5.16}$$

$$S(p, L) \propto L^{\gamma/\nu} S[(p - p_c)L^{-1/\nu}], \tag{5.17}$$

where Π is the percolation probability, P is the probability that a randomly chosen site belongs the the percolating cluster and S is the mean cluster size. The percolating cluster has fractal behavior related to its density $\rho(r)$ at various length r

$$\rho(r) \sim r^{D-d}. \tag{5.18}$$

This behavior is expected for percolating cluster at critical point.

5.3.4 Fractal growth phenomena

The fractal behavior of a system is not only a characteristic of the critical point but its the signature of a specific process of aggregation. There are two main class of process of aggregation the Diffusion Limited Aggregation (DLA) and the Cluster Cluster Aggregation [49].

Diffusion Limited Aggregation

The process starts with a particle in the center of a lattice. A second particle diffuses randomly on the lattice until it will meet the first particle. After the collision the second particle attaches to the first and a third diffusive particle is introduced in the lattice and the process continues. The DLA fractal dimension is:

- $D = 1.70 \pm 0.06$ for $d = 2$
- $D = 2.53 \pm 0.06$ for $d = 3$

Cluster cluster aggregation

This process characterize the aggregation of particles which diffuse in a medium. Each particle has a probability to bind another after a collision. There are different regimes for Cluster Cluster aggregation for different potential of interaction. If the interaction has a deep minimum and a small repulsive barrier, the process is called "diffusion limited". In this case, if two cluster collides they aggregate in a time necessary for a contact. This regime is characterized by the following fractal dimensions:

- $D = 1.44 \pm 0.03$ for $d = 2$
- $D = 1.78 \pm 0.06$ for $d = 3$
- $D = 2.07 \pm 0.1$ for $d = 4$

If there is an important contribute to the repulsive part of potential, the process is "reaction limited". After the binding of some clusters the aggregation of other cluster is inhibited, but if it happens after an higher contact number, the binding is permanent. The characteristic time is the time to form a binding. The regime "Cluster-Cluster reversible" happens when the clusters can dissociate and reorganize.

5.4 Monte Carlo results

We perform Monte Carlo simulations of system with boundary periodic conditions starting from cells in random positions on square lattice of linear dimension $L = 64, 128, 256, 512$, corresponding to simulate systems of linear size $L \sim 0.2mm, 0.4mm, 0.8mm, 1.5mm$. Usually the experimental matrix gel have a linear size of order of $\sim 1mm$. We consider the equilibrium structure after a number of MCS which is sufficient to reaches stable structures. This time is between 1000 and 5000 MCS, the first for the smaller size and

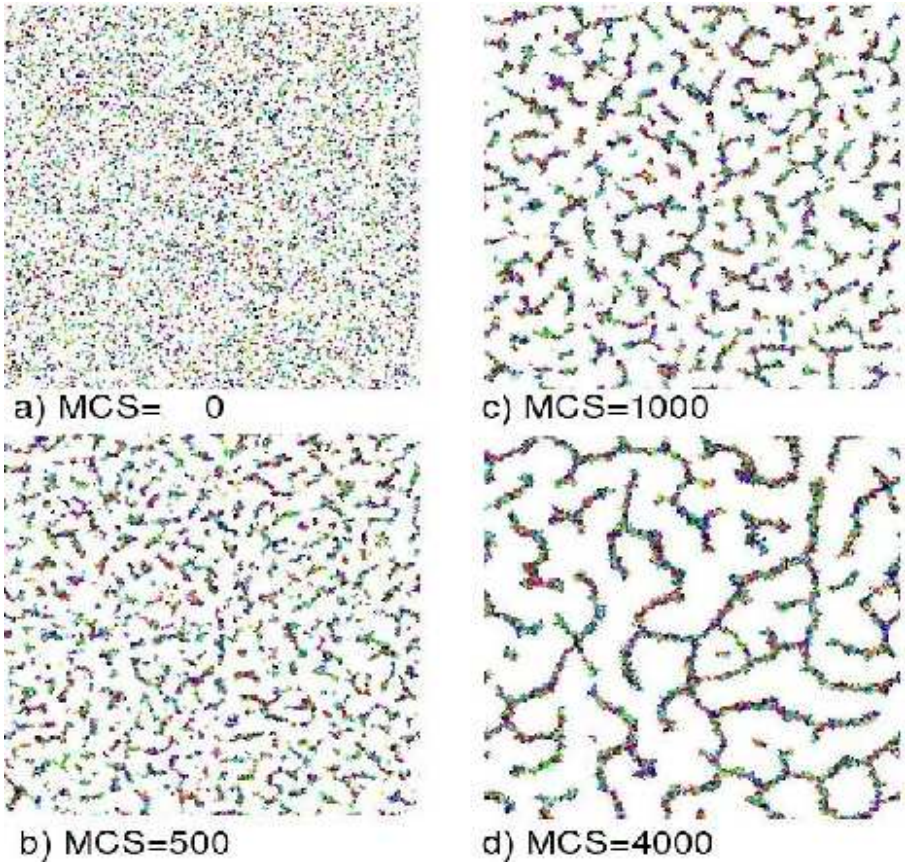

Figure 5.3: Pictures of vascular structures obtained from simulations at different time. a) MCS = 0 $\sim$ 0 h; b) MCS = 500 $\sim$ 4h; c) MCS = 1000 $\sim$ 10h; d) MCS = 4000 $\sim$ 40h.

the last for the largest size. The MCS time corresponds to a real time between ~ 8 hours and ~ 40 hours. In Fig. 5.3 is show an example of simulated system at different time.

We want to investigate to role of attractant effective radius on the fractal behavior of structures, then we perform simulation for different values of ϵ the degradation rate of chemotactic factor, corresponding to $r_0 \sim 10\mu m, \sim 20\mu m, \sim 200\mu m$. Form now on we refer to r_0 always in unit of μm.

First of all we individuate the critical density p_c for the percolative transition. Using the scaling invariance at critical point we calculate p_c from the intersection point of percolation probability curves obtained for different size of system Fig. 5.4. The critical density is $p_c \sim 0.2$ with small differences between the three values of r_0.

Fractal dimension

At critical point we measured the fractal dimension of percolating cluster using the sandbox method. It consists in choosing a point of percolating cluster and measuring the density of percolating cluster inside spheres of increasing radius. To have a good measure of density of percolating cluster $\rho(r)$, we start from different point of some cluster and made the average value for each radius. This is convenient method to estimate the fractal dimension using Eq. (5.18). The behavior of fractal dimension for different r_0 is showed in Fig. 5.5. The functions show clearly the presence of two different regimes in fractal dimension. At small scales the clusters are characterized of a fractal dimension close to the cluster-cluster aggregation in the regime diffusion limited. In particular

- D $= 1.50 \pm 0.05$, for $r_0 \sim 10$;
- D $= 1.44 \pm 0.04$, for $r_0 \sim 20$;
- D $= 1.45 \pm 0.04$, for $r_0 \sim 200$;

For higher scales the fractal dimension is D=1.87 $\pm$0.03 which is compatible with random percolation. The crossover point in the scale between the two behaviors is proportional to the effective interaction radius r_0.

In our simulation for $r_0 > 200$ we obtain the same behavior of fractal dimension of $r_0 = 200$, the crossover point doesn't increases any more. This effect is probably duo to the finite length of L. Then our simulation has to be intended as an indications of behavior of fractal dimension for different r_0. The Simulated structures suggest that for scales where the influence of the affective attractant radius is important the dynamical process of cluster formation is cluster cluster aggregation. In cluster-cluster aggregation it is assumed that starting from random initial positions the particles can diffuse

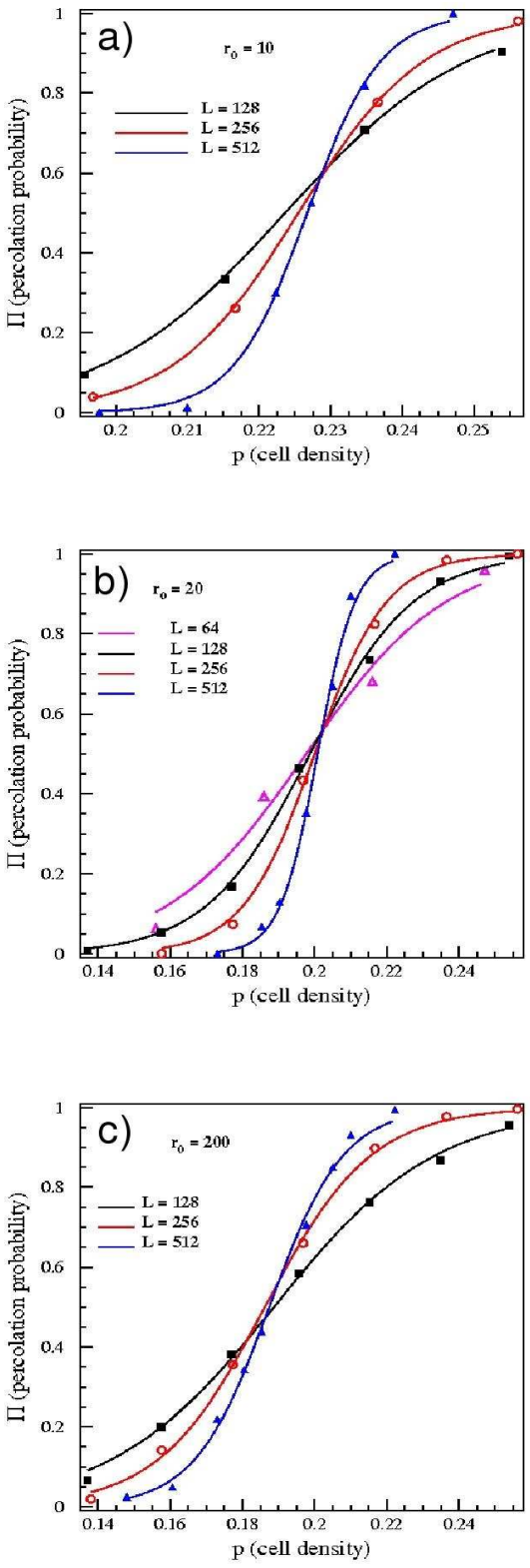

Figure 5.4: Percolation probability as function of cell density for different size L at three different values of r_0. a)$r_0 \sim 10$ the percolation threshold is $p_c = 0.228 \pm 0.005$; b)$r_0 \sim 20$ the percolation threshold is $p_c = 0.201 \pm 0.005$; b)$r_0 \sim 200$ the percolation threshold is $p_c = 0.18 \pm 0.01$. For each point we compute 150 - 300 realizations of the system, starting from random initial conditions. The percolation threshold shows a slightly dependence on the attractant radius. The curves are only guides for eye.

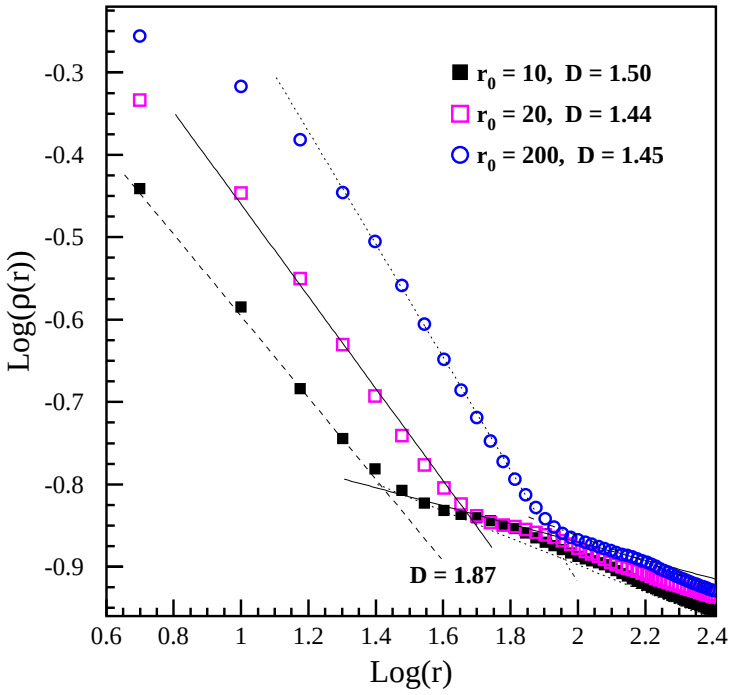

Figure 5.5: Density of percolating cluster as function of radius for the three different r_0.

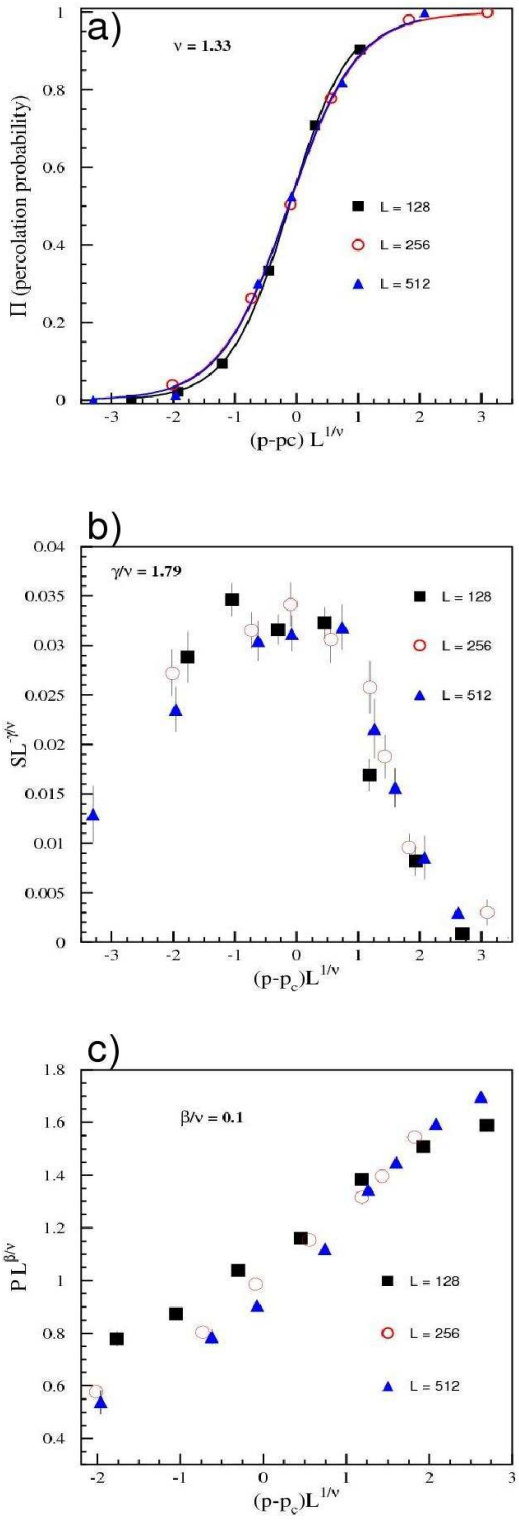

Figure 5.6: Data collapse of a)percolation probabilityΠ, b)mean cluster size S and c)the probability to belong to percolating cluster P.

according some rules and stick with a given probability when they get in touch. In this work, although the particles have not purely diffusive motion but a also a directed motion because of gradient of attractant, they presents the fractal dimension of cluster-cluster aggregation.

For higher scale the aggregation process is mainly determined by initial random positioning of the cells without alteration from dynamical process of migration.

Other critical index for $L \gg r_0$

To better understand the critical behavior for scales large respect to r_0 we measure the critical index ν, β and γ for $r_0 \sim 10$. We showed that these index regulate the critical behavior of the percolation probability Π, the probability to belong to percolating cluster P and the mean cluster size S by the scaling equations.

Using the scaling Eqs. (5.15), (5.16), (5.17) we estimate the critical index by data collapse (Fig. 5.6). Using the values of random percolation, the curves have a good collapse. This confirms the hypothesis that, for very large scales respect to effective interaction length produced by chemoattractant, the fractal behavior is determined only by the random initial conditions.

5.5 Discussion

In this chapter we studied the fractal behavior of simulated vascular networks using the Cellular Potts Model [39]. The model simulates, toward a lattice-gas Hamiltonian, a distribution of endothelial cells which auto-organize under the influence of an autocrine chemotactic factor. The chemoattractant is simulated by a continuous density produced by cells and its secretion, degradation and diffusion is regulated by a diffusion equation. The root square of diffusivity times the degradation rate offer a natural length scale of the effective attractant radius r_0.

The study was performed to investigate the dependence of fractal behavior as function of r_0. From our simulation it is evident that for each r_0 there are of two different regimes in fractal dimension. For small scales, the fractal behavior is strictly linked to the dynamical mechanism of cell cell aggregation. For longer scale the critical behavior is regulated by initial random conditions producing a fractal dimension which is compatible with random percolation. The behavior of random percolation at large scale is also confirmed by the values of critical index which regulate the behavior of Π, P and S. The chemotactic factor mediates the interaction between cells and a measure of the interaction length is r_0 which characterizes the scale for the dynamical aggregation process. At scale where the value of r_0 is relevant, the

value of fractal dimension is close to the ones of cluster-cluster aggregation in the regime diffusion limited. The crossover between the two behaviors is proportional to r_0.

Conclusion

We have presented a Statistical Mechanics approach to the study of Eukaryotic Directional Sensing.

Starting from the observation of a phase separation between signaling molecules in the process of Directional Sensing, we modeled it by standard statistical mechanics method. We have used Monte Carlo simulations of a spin lattice model regulated by an effective free energy, to represent the interaction between enzymes, with an enzymatic reservoir and with an external activation field. The model maps the cell surface on a square lattice and enzymes on a spin variable. The effective interaction between enzymes on the membrane is represented by a ferromagnetic short range coupling, the interaction of the enzymes with an external chemoattractant is modeled by an interaction with an external magnetic field and a long-range antiferromagnetic interaction plays the role of the interaction with a cytosolic reservoir. The interplay between the long-range antiferromagnetic interaction (enzymes shuttling from the cytosolic reservoir to the membrane) and the effect of the external activation field introduce a feedback mechanism which leads to a self-organization process. In fact is shown that it provides a self-tuning mechanism, which drives the system towards phase coexistence and polarization. The model reproduces important aspects of the observed phenomenology, and sheds light on the underlying physical mechanism. The organization of signaling molecules is modeled as a coarsening process of spin domains, and the polarized state corresponds to the phase separation. It predicts power law dependence of the polarization time as function of the gradient of external chemoattractant. In particular there are of two distinct time behaviors in cluster evolution. When an attractant gradient is present it is signaled, in the model simulations, by the emergence of a double power law for the time evolution of clusters of signaling molecules. In absence of an external gradient the cluster size simply evolves in time as $t^{1/2}$. Our results are based on fundamentals elements of Statistical Mechanics and, although they were inspired by the particular biochemical mechanism described in [4], they are mostly independent on the details of the underlying reaction network.

In the second part, we have studied the Hamiltonian of the lattice model in a continuous formalism deriving the associated Ginzburg-Landau functional in the framework of large N limit. We focalized on the phase ordering process taking place for sub-critical temperature in presence of an external field. We analyzed the Langevin motion equations and derived the phase diagram of the system. The resulting phase diagram in the plane (T, h), where T is the temperature and h the magnetic field, shows an expansion of the phase coexistence region outside the $h = 0$ region. The amplitude of phase coexistence region increases with the increasing of the antiferromagnetic coupling. For sub-critical temperature a condensation of fluctuations at $k = k_{0^+}$ takes place. This mechanism, similar to the Bose-Einstein condensation, is the manifestation of a phase separation process. We have also studied the time behavior of magnetization which is in agreement with the Monte Carlo simulations and the time behavior of fluctuations which is a power law with a growth exponent 1/2. The investigated general properties of the self-tuning mechanism of magnetization on phase coexistence can be relevant in the study of other systems.

Finally we studied the fractal behavior of simulated vascular networks as function of the interaction radius of the chemoattractant. From our simulations it is evident that there are two regimes characterized by two different fractal dimensions. For small scales, the fractal behavior is strictly linked to the dynamical mechanism of cell-cell aggregation. For longer scale the critical behavior is regulated by initial random conditions producing a fractal dimension which is compatible with random percolation. The chemotactic factor mediates the interaction between cells and for scales smaller than the interaction length the dynamical aggregation process is a cluster-cluster aggregation. For larger scales the aggregation is regulated by the initial random position of the cells.

Appendix A

Fourier transform

In this section we report the conventions adopted to calculate the Fourier Transform used in chapter 3 and in chapter 4.

$$\vec{\phi}(\vec{k}) = \int_V d\vec{x}\vec{\phi}(\vec{x})e^{i\vec{k}\cdot\vec{x}} \tag{A.1}$$

$$\vec{\phi}(\vec{x}) = \frac{1}{V}\sum_{\vec{k}} \vec{\phi}(\vec{k})e^{-i\vec{k}\cdot\vec{x}} \tag{A.2}$$

$$\frac{1}{V}\sum_{\vec{k}} \vec{\phi}(\vec{k})e^{i\vec{k}\cdot(\vec{x}-\vec{x}')} = \delta(\vec{x}-\vec{x}') \tag{A.3}$$

$$\int_V d\vec{x}e^{i\vec{x}\cdot(\vec{k}-\vec{k}')} = V\delta_{\vec{k},\vec{k}'} \tag{A.4}$$

Appendix B

Equations of the motion for non-uniform h

Let us consider a non uniform magnetic field $h(\vec{x})$. We start from the equations 3.22 and 3.23:

$$\begin{aligned}\frac{\partial m(\vec{x},t)}{\partial t} &= -(-\nabla^2 + r)m(\vec{x},t) - \frac{\lambda}{V}\int m(\vec{x},t)d^d\vec{x} + \\ &\quad -\frac{g}{N}m^2(\vec{x},t) - \frac{g}{N}(\phi_\perp \cdot \phi_\perp)m(\vec{x},t) + h(\vec{x}) \qquad \text{(B.1)}\end{aligned}$$

$$\begin{aligned}\frac{\partial \phi_\perp(\vec{x},t)}{\partial t} &= -(-\nabla^2 + r)\phi_\perp(\vec{x},t) - \frac{g}{N}m^2(\vec{x},t)\phi_\perp(\vec{x},t) + \\ &\quad -\frac{g}{N}(\phi_\perp(\vec{x},t) \cdot \phi_\perp(\vec{x},t))\phi_\perp(\vec{x},t) \\ &\quad -\frac{\lambda}{V}\int_V d\vec{x}\phi_\perp(\vec{x},t) + \eta_\perp(\vec{x},t) \qquad \text{(B.2)}\end{aligned}$$

In the limit $N \to \infty$ we obtain:

$$\frac{1}{N}(\phi_\perp(\vec{x},t) \cdot \phi_\perp(\vec{x},t)) \to S(\vec{x},t) = \frac{1}{N}\langle \phi_\perp(\vec{x},t) \cdot \phi_\perp(\vec{x},t)\rangle. \qquad \text{(B.3)}$$

Using the Eq. (A.2) it is valid for $S(\vec{x},t)$ the following expression:

$$S(\vec{x},t) = \frac{1}{NV^2}\sum_{\vec{k}_1,\vec{k}_2}\langle \phi_\perp(\vec{k}_1,t)\phi_\perp(\vec{k}_2,t)\rangle e^{-i(\vec{k}_1+\vec{k}_2)\cdot\vec{x}}. \qquad \text{(B.4)}$$

We define the transverse structure factor:

$$C(\vec{k}_1,\vec{k}_2,t) = \frac{1}{N}\langle \phi_\perp(\vec{k}_1,t) \cdot \phi_\perp(\vec{k}_2,t)\rangle \qquad \text{(B.5)}$$

After Fourier transform of B.1 and B.2 (we indicate with $\phi(\vec{k},t)$ the orthogonal component of the field $\vec{\phi}_\perp(\vec{k},t)$):

$$\begin{aligned}\frac{\partial m(\vec{k},t)}{\partial t} &= -(k^2+r)m(\vec{k},t) - \lambda m(0,t)\delta_{\vec{k},0} + \\ &\quad -\frac{1}{V^2}\frac{g}{N}\sum_{\vec{k}_2,\vec{k}_3} m(\vec{k}-\vec{k}_2-\vec{k}_3,t)m(\vec{k}_2,t)m(\vec{k}_3,t) \\ &\quad -\frac{g}{V^2}\sum_{\vec{k}_2,\vec{k}_3} C(\vec{k}-\vec{k}_2-\vec{k}_3,\vec{k}_2,t)m(\vec{k}_3,t) + h(\vec{k}) \qquad \text{(B.6)}\end{aligned}$$

$$\begin{aligned}\frac{\partial \phi(\vec{k},t)}{\partial t} &= -(k^2+r)\phi(\vec{k},t) - \lambda\phi(0,t)\delta_{\vec{k},0} + \\ &\quad -\frac{1}{V^2}\frac{g}{N}\sum_{\vec{k}_2,\vec{k}_3} m(\vec{k}-\vec{k}_2-\vec{k}_3,t)m(\vec{k}_2,t)\phi(\vec{k}_3,t) + \\ &\quad -\frac{1}{V^2}g\sum_{\vec{k}_2,\vec{k}_3}\langle\phi(\vec{k}-\vec{k}_2-\vec{k}_3,t)\phi(\vec{k}_2,t)\rangle\phi(\vec{k}_3,t) + \eta_\perp(\vec{k},t) \qquad \text{(B.7)}\end{aligned}$$

The motion equation for $C(\vec{k}_1,\vec{k}_2,t)$ can be obtained calculating $C(\vec{k}_1,\vec{k}_2,t) = \langle\phi(\vec{k}_1,t)\phi(\vec{k}_2,t)\rangle$:

$$\frac{\partial C(\vec{k}_1,\vec{k}_2,t)}{\partial t} = \langle\frac{\partial\phi(\vec{k}_1,t)}{\partial t}\phi(\vec{k}_2,t) + \phi(\vec{k}_1,t)\frac{\partial\phi(\vec{k}_2,t)}{\partial t}\rangle, \qquad \text{(B.8)}$$

substituting B.7 in B.8:

$$\begin{aligned}\frac{\partial C(\vec{k}_1,\vec{k}_2,t)}{\partial t} &= -(k_1^2+k_2^2+2r)\langle\phi(\vec{k}_1,t)\phi(\vec{k}_2,t)\rangle \\ &\quad -\lambda(\langle\phi(0,t)\phi(\vec{k}_2,t)\rangle\delta_{\vec{k}_1,0} + \langle\phi(0,t)\phi(\vec{k}_1,t)\rangle\delta_{\vec{k}_2,0}) + \\ &\quad -\frac{1}{V^2}\frac{g}{N}\sum_{\vec{p},\vec{q}} m(\vec{k}_1-\vec{p}-\vec{q},t)m(\vec{p},t)\langle\phi(\vec{q},t)\phi(\vec{k}_2,t)\rangle + \\ &\quad -\frac{1}{V^2}\frac{g}{N}\sum_{\vec{p},\vec{q}} m(\vec{k}_2-\vec{p}-\vec{q},t)m(\vec{p},t)\langle\phi(\vec{q},t)\phi(\vec{k}_1,t)\rangle + \\ &\quad -\frac{1}{V^2}g\sum_{\vec{p},\vec{q}}\langle\phi(\vec{k}_1-\vec{p}-\vec{q},t)\phi(\vec{p},t)\rangle\langle\phi(\vec{q},t)\phi(\vec{k}_2,t)\rangle + \\ &\quad -\frac{1}{V^2}g\sum_{\vec{p},\vec{q}}\langle\phi(\vec{k}_2-\vec{p}-\vec{q},t)\phi(\vec{p},t)\rangle\langle\phi(\vec{q},t)\phi(\vec{k}_1,t)\rangle + \\ &\quad +\langle\eta_\perp(\vec{k}_1,t)\phi(\vec{k}_2,t)\rangle + \langle\eta_\perp(\vec{k}_2,t)\phi(\vec{k}_1,t)\rangle. \qquad \text{(B.9)}\end{aligned}$$

Is is useful to write the convolutions as follows:

$$\begin{aligned}\sum_{\vec{k}_2,\vec{k}_3}\langle\phi(\vec{k}-\vec{k}_2-\vec{k}_3,t)\phi(\vec{k}_2,t)\rangle m(\vec{k}_3,t) &= \\ \sum_{\vec{k}_3}(\sum_{\vec{k}_2}\langle\phi(\vec{k}-\vec{k}_2-\vec{k}_3,t)\phi(\vec{k}_2,t)\rangle)m(\vec{k}_3,t) &= \\ V\sum_{\vec{k}_3}S(\vec{k}-\vec{k}_3)m(\vec{k}_3,t), & \qquad \text{(B.10)}\end{aligned}$$

where

$$S(\vec{k}-\vec{k}_3)=\frac{1}{V}\sum_{\vec{k}_2}\langle\phi(\vec{k}-\vec{k}_2-\vec{k}_3,t)\phi(\vec{k}_2,t)\rangle \qquad \text{(B.11)}$$

then:

$$\begin{aligned}\frac{\partial C(\vec{k}_1,\vec{k}_2,t)}{\partial t} &= -(k_1^2+k_2^2+2r)C(\vec{k}_1,\vec{k}_2,t)-\lambda[C(0,k_2,t)\delta_{\vec{k}_1,0}+C(0,k_1,t)\delta_{\vec{k}_2,0}]+ \\ &-\frac{1}{V^2}\frac{g}{N}\sum_{\vec{p},\vec{q}}m(\vec{k}_1-\vec{p}-\vec{q},t)m(\vec{p},t)C(\vec{q},\vec{k}_2,t)+ \\ &-\frac{1}{V^2}\frac{g}{N}\sum_{\vec{p},\vec{q}}m(\vec{k}_2-\vec{p}-\vec{q},t)m(\vec{p},t)C(\vec{q},\vec{k}_1,t)+ \\ &-\frac{1}{V}g\sum_{\vec{q}}S(\vec{k}_1-\vec{q},t)C(\vec{q},\vec{k}_2,t)+ \\ &-\frac{1}{V}g\sum_{\vec{q}}S(\vec{k}_2-\vec{q},t)C(\vec{q},\vec{k}_1,t)+ \\ &+\langle\eta_\perp(\vec{k}_1,t)\phi(\vec{k}_2,t)\rangle+\langle\eta_\perp(\vec{k}_2,t)\phi(\vec{k}_1,t)\rangle \qquad \text{(B.12)}\end{aligned}$$

in the case of small anisotropy we can assume the isotropy of noise namely:

$$\langle\eta_\perp(\vec{k}_1,t)\phi(\vec{k}_2,t)\rangle+\langle\eta_\perp(\vec{k}_2,t)\phi(\vec{k}_1,t)\rangle=2VT\delta_{\vec{k}_1+\vec{k}_2} \qquad \text{(B.13)}$$

let us remember the equation for magnetization:

$$\begin{aligned}\frac{\partial m(\vec{k},t)}{\partial t} &= -(k^2+r)m(\vec{k},t)-\lambda m(0,t)\delta_{\vec{k},0}+ \\ &-\frac{1}{V^2}\frac{g}{N}\sum_{\vec{p},\vec{q}}m(\vec{k}-\vec{p}-\vec{q},t)m(\vec{p},t)m(\vec{q},t)+ \\ &-\frac{1}{V}g\sum_{\vec{q}}S(\vec{k}-\vec{q},t)m(\vec{q},t)+h(\vec{k}) \qquad \text{(B.14)}\end{aligned}$$

close the system the auto-consistence relation:

$$S(\vec{k}-\vec{q},t) = \frac{1}{V}\sum_{\vec{p}} C(\vec{k}-\vec{p}-\vec{q},\vec{p},t). \tag{B.15}$$

Appendix C

Monte Carlo simulations

In the last years computer simulations and numerical methods have revested a fundamental role in the investigation of complex systems.

The simulations let measure a wide class of properties, ranging from local to macroscopic quantities, providing a direct comparison between model results and experiments.

The Monte Carlo method [50] results to be very useful when studying systems whose motion equation are complicated and difficult to be solved. By means of Monte Carlo simulations, the probability distribution which defines the ensamble of system states is directly sampled introducing an "effective" dynamics.

The thermal average of an observable $A(\mathbf{x})$, where $\mathbf{x}$ is a vector in phase space describing the considered degrees of freedom, is defined as:

$$\langle A(\mathbf{x})\rangle = \frac{1}{Z}\int \exp\left[-\mathcal{H}(\mathbf{x})/k_BT\right] A(\mathbf{x})d\mathbf{x}, \tag{C.1}$$

where

$$Z = \int \exp\left[\mathcal{H}(\mathbf{x})/k_BT\right] d\mathbf{x} \tag{C.2}$$

is the partition function, and $\mathcal{H}(\mathbf{x})$ is the Hamiltonian of the model. The normalized Boltzmann factor $P(\mathbf{x}) = \exp\left[\mathcal{H}(\mathbf{x})/k_BT\right]/Z$ plays the role of a probability density, representing the statistical weight with which the configuration $\mathbf{x}$ occurs in thermal equilibrium. Within the Monte Carlo method, the exact Eq. C.1 is approximated with the sum over a subset of phase space points $\{\mathbf{x}_1, \mathbf{x}_2, ..., \mathbf{x}_M\}$, which are used as statistical sample. Clearly, the discrete sum

$$\overline{A(\mathbf{x})} = \frac{\sum_{l=1}^{M} \exp\left[-\mathcal{H}(\mathbf{x}_l)/k_BT\right] A(\mathbf{x}_l)}{\sum_{l=1}^{M} \exp\left[-\mathcal{H}(\mathbf{x}_l)/k_BT\right]} \tag{C.3}$$

must approximate Eq. C.1 in the limit $M \to \infty$. It can be shown that $\overline{A} =< A > +O(N^{-1/2})$ [51].

The dynamics arising from Monte Carlo simulation moves along the discrete set of phase space variables $\{\mathbf{x}_1, \mathbf{x}_2, ..., \mathbf{x}_M\}$: it takes place in discrete time steps, each $\mathbf{x}_i$ univocally determines the probability distribution of the successive state, and such probability does not depend on time explicitly. Metropolis et al. [52] advanced the idea to choose the successive states $\{\mathbf{x}_l\}$ building a Markov process, where each state $\mathbf{x}_{i+1}$ is constructed from the previous $\mathbf{x}_i$ via a suitable transition probability $W(\mathbf{x}_i \to \mathbf{x}_{i+1})$. They pointed out that it is possible to choose the transition probability W such that in the limit $M \to \infty$ the distribution function $P(\mathbf{x}_l)$ generated by this Markov process tends towards the desired equilibrium distribution $P_{eq}(\mathbf{x}_l)$:

$$P_{eq}(\mathbf{x}_l) = \frac{1}{Z} \exp\left(-\frac{\mathcal{H}(\mathbf{x}_l)}{k_B T}\right). \tag{C.4}$$

To achieve this issue, it is sufficient to impose the principle of detailed balance:

$$P_{eq}(\mathbf{x}_l) W(\mathbf{x}_l \to \mathbf{x}_{l'}) = P_{eq}(\mathbf{x}_{l'}) W(\mathbf{x}_{l'} \to \mathbf{x}_l). \tag{C.5}$$

Using Eq. C.4 and Eq. C.5 we obtain:

$$\frac{W(\mathbf{x}_l \to \mathbf{x}_{l'})}{W(\mathbf{x}_{l'} \to \mathbf{x}_l)} = \exp\left(-\frac{\delta\mathcal{H}}{k_B T}\right), \tag{C.6}$$

where $\delta\mathcal{H} = \mathcal{H}(\mathbf{x}_{l'}) - \mathcal{H}(\mathbf{x}_l)$ is the energy variation. The latter equation does not fix the transition probability uniquely, and some arbitrariness in the explicit choice of W remains. One of the most common used expression of the transition probability is the following:

$$W(\mathbf{x}_l \to \mathbf{x}_{l'}) = \begin{cases} \exp\left(-\delta\mathcal{H}/k_B T\right)/\tau_s & \text{if } \delta\mathcal{H} > 0 \\ 1/\tau_s & \text{otherwise} \end{cases}$$

where τ_s is an arbitrary factor, representing the unit of Monte Carlo time. Hence W is the transition probability per unit time [50].

Appendix D

Phase transitions and critical exponents

Phase transition are phenomena of sharp variation of behavior of a physical system in response to the variation of some parameters. For a gas the variation of the density produce the liquid, a quench in the temperature for $T \to T_c$ produce in a magnetic material the transition from the paramagnetic state to the ferromagnetic state.

In a phase transition there are phenomena of symmetry breaking. The ordered phase has an inferior degree of symmetry respect to the Hamiltonian of the system. A classical example the formation of a spontaneous magnetization in a ferromagnet. The spontaneous magnetization gives to the system a particular direction but its Hamiltonian is isotropic.

To describe the phase transitions Landau introduced the order parameter as measure of the degree of the order in a system. For a ferromagnet a good order parameter is the density of magnetization, for a gas-liquid transition the difference of the density between the liquid and gas phase describes very well the ordering process.

It is important to measure the variation of the order parameter after an infinitesimal variation of an external field i. e.:

$$\chi = \frac{\partial OrderParameter}{\partial ExternalField}. \tag{D.1}$$

Thanks to the fluctuation-dissipation theorem we can say that the fluctuation of the order parameter are proportional to χ.

If the order parameter is defined as $\langle\sigma\rangle$ we can define a correlation function as:

$$c_{ij} = \langle(\sigma_i - \langle\sigma_i\rangle)(\sigma_j - \langle\sigma_j\rangle)\rangle \tag{D.2}$$

After a correlation function we can define a correlation length which define the linear dimension of fluctuations:

$$\xi^2 = \frac{\sum r^2 c(r)}{\sum c(r)} \tag{D.3}$$

where r is the distance between i and j.

The behavior of the order parameter, susceptivity and correlation length at critical point allows to divide the phase transitions in too big classes. We can distinguish the first order phase transition, characterized by a discontinuity of order parameter and finite χ and ξ at critical point. The second order phase transition has no discontinuity in the order parameter but the the order parameter approaches to zero at critical point and, at some time, $\xi \to \infty$ and $\chi \to \infty$.

These behavior have a quantitative characterization in the critical index:

$$Orderparameter \sim \epsilon^{\beta} \; if \epsilon > 0, \tag{D.4}$$

$$\chi \sim |\epsilon|^{-\gamma}, \tag{D.5}$$

$$\xi \sim |\epsilon|^{-\nu}, \tag{D.6}$$

where $\epsilon = \frac{T - T_c}{T}$ if the phase transition is determined by temperature. The specific heat has a singularity at critical point

$$C_V \sim |\epsilon|^{-\alpha}, \tag{D.7}$$

and correlation function goes as:

$$c(r) \sim |\epsilon|^{-\eta}. \tag{D.8}$$

The critical exponent are very important because they characterize the critical behavior. Systems very different each other and very complex can have the some critical exponents. It is demonstrated that only two exponents are independent because they are related by *scaling relations*:

$$\alpha + 2\beta + \gamma = 2, \tag{D.9}$$

$$2 - \eta = \frac{\gamma}{\nu} \tag{D.10}$$

and the *hyperscaling relations* which involves the euclidean spatial dimension d:

$$2 - \alpha = \nu d. \tag{D.11}$$

The previous scaling relations are founded on scaling hypothesis [36], which is also the basis of renormalization theory. This hypothesis consists in the idea that at critical point the phenomena are dominated by the fluctuation on large scale, measured by ξ. The details of the interactions are not important, the system is characterized only by the global properties:

- spatial dimension d;
- dimension of order parameter;
- symmetries of Hamiltonian.

The critical exponents individuates large classes of phase transitions, called universality class. The universality is the fundamental idea of modelling complicated systems by simplified scheme. The critical behavior is in fact independent by the details of interactions.

Bibliography

[1] C. Janetopoulos *et al.*, Proc. Natl. Acad. Sci. U.S.A. **101**, 8951 (2004).

[2] A. Ridley *et al.*, Science **302**, 5651 (2003).

[3] D.A. Lauffenburger and A.F. Horwitz, Cell **84**, 359 (1996).

[4] A. Gamba, *et al.* Proc. Natl. Acad. Sci U.S.A. **102**, 16927 (2005).

[5] A. de Candia *et al.*, Sci. STKE **378**, pl1 (2007).

[6] M. Iijima and P. Devreotes, Cell **109**, 599 (2002).

[7] M. Dance *et al.*, J. Biol. Chem. **281**, 23285 (2006).

[8] S.H. Zigmond, J. Cell. Biol. **75**, 606 (1977).

[9] E.M. Lifshitz, and L.P. Pitaevskii, *Physical Kinetics* (Pergamon Press, 1981).

[10] L. Song *et al.*, Eur. J. Cell Biol. **85**, 981 (2006).

[11] C. Janetopoulos *et al.*, Proc. Natl. Acad. Sci. U.S.A. **101**, 16606 (2004).

[12] A. Bray, Adv. Phys. **45**, 357 (1994).

[13] A. Gamba *et al.*, Phys. Rev. Lett. (2007).

[14] P. Devreotes and C. Janetopoulos, J. Biol. Chem. **278**, 20445 (2003).

[15] M. Postma *et al.*, J. Cell. Sci. **117**,2925 (2004).

[16] H. Levine *et al.*, Proc. Natl. Acad. Sci U.S.A. **103**, 9761 (2006).

[17] M. Meier-Schellersheim *et al.*, PLoS **2**, e82, 0710 (2006).

[18] P. A. Iglesias and P. N. Devreotes, Curr. Opinion in Cell Biol. (in press), **20** (2008).

[19] T. Pollard and G. G. Borisy, Cell, **112**, 453, (2003).

[20] J. V. Small *et al.*, Nature **272**, 638, (1978).

[21] L. Ma *et al.*, Biophysical Journal, **87**, 3764, 2004.

[22] M. Onsun and C. V. Rao, PLoS **3**, e36, 0436 (2007).

[23] T. Ferraro *et al.*, Europhysics Letters, **83**, 50009, 2008.

[24] R. Ananthakrishnan and A. Ehrlicher, Int. J. Biol. Sci., **3**, 303, 2007.

[25] E. Stanley, *introduction to phase transition and critical phenomena*, Oxford University Press, 1971

[26] P. M. Chaikin and T.C. Lubensky *Principles of condensed matter physics*, Cambridge University Press, 1995

[27] A. Coniglio, P. Ruggiero and M. Zannetti, Phys. Rev. E, **50**, 1046, 1994

[28] J. D. Gunton *phase transition and critical phenomena*, vol 6

[29] Numerical Recipes, Cambridge University Press.

[30] M. Zannetti, J. Phys. A Math. Gen. **26**, 3037, 1993.

[31] C.Castellano, F.Corberi and M.Zannetti, Phys. Rev. E, **56**, 4973 (1997).

[32] N.Fusco and M.Zannetti, Phys. Rev. E, **66**, 066113 (2002).

[33] P. J. Flory, J. Am. Chem. Soc., **63**, 3083, (1941).

[34] W. H. Stockmayer, J. Chem. Phys., **11**, 45 (1943).

[35] D. Stauffer and A. Aharony, *Introduction to Percolation Theory*, Taylor Francis, London, (1994).

[36] L. P. Kadanoff *et al.*, Rev. Mod. Phys., **39**, 395, (1967)

[37] F. Graner and J. Glazier, Phys. Rev. Lett., **69**, 2013, (1992)

[38] J. Glazier an F. Graner, Phys. Rev. E, **47**, 2128, (1992)

[39] R. M. H. Merks *et al.*, Developmental Biology, **289**, 44, (2006)

[40] A. Gamba *et al.*, Phys. Rev. Lett., **90**, 118101, (2003)

[41] A. Coniglio *et al.*, Phys. Rev. E, **69**, 51910, (2004)

[42] G. Serini *et al.*, EMBO J., **22**, 1771, (2003)

[43] D. Manoussaki *et al.*, Acta Biothereol, **44**, 271, (1996)

[44] A. Szabo *et al.*, Phys. Rev. Lett., **98**, 38102, (2007)

[45] P. Carmeliet, Nat. Med., **6**, 389, (2000).

[46] D. Guidolin *et al.*, Leukemia **18**, 1745, (2004).

[47] C. Ruhrberg *et al.*, Genes and Development **16**, 2684, (2002).

[48] P. G. Vico *et al.*, J. Theoreticl Biology **195**, 525, (1998).

[49] Tamas Vicsek, *Fractal growth phenomena*, World Scientific, (1989).

[50] K. Binder, D. W. Hermann, *Monte Carlo Simulation in Statistical Physics*, Springer-Verlag, Berlin (1988).

[51] L. Peliti, *Appunti di Meccanica Statistica*, Bollati Boringhieri, Torino (2003).

[52] N. Metropolis, A. W. Rosenbluth, M. N. Rosenbluth, A. H. Teller, E. Teller, *J. Chem. Phys.* **21**, 1087 (1953).

Acknowledgments

I would like to thank Dr. Antonio De Candia, Prof. Antonio Coniglio and Dr. Andrea Gamba for the great support and fruitful discussions which helped me in many occasions.

It is a great pleasure for me to thank Prof. Marco Zannetti which teached me, with great patience, analytical methods.

A special thank for Prof. Luca Peliti for the interesting discussions and his careful suggestions.

I am grateful to Guido Celentano for his incredible capacity to understand and listen me.

I would also like to express my gratitude for scientific discussion and human support to: Tiziana Abete, Emanuela Del Gado, Alberto Imparato, Prof. Lucilla de Arcangelis, Annalisa Fierro and Massimo Picaciamarra.

I don't want to close my acknowledgments without to thank all my friends and Luca which shared with me the joy and sadness of the last three years.